This article has been accepted for publication in a future issue of this journal, but has not been fully edited. Content may change prior to final publication. Citation information: DOI 10.1109/ACCESS.2017.2733557, IEEE Access

Quantum-Assisted Indoor Localization for Uplink mm-Wave and Downlink Visible Light Communication Systems

Panagiotis Botsinis, *Member, IEEE,* Dimitrios Alanis, *Student Member, IEEE,* Simeng Feng, Zunaira Babar, Hung Nguyen, *Member, IEEE,* Daryus Chandra, Soon Xin Ng, *Senior Member, IEEE,* Rong Zhang, *Senior Member, IEEE,* and Lajos Hanzo, *Fellow, IEEE*

***Abstract*—With the proliferation of mm-Wave systems and Visible Light Communications (VLC), indoor localization may find multiple applications. When high localization accuracy is required and triangulation is not possible due to the infrastracture and scenario limitations, the computational complexity of searching on a virtual grid may become excessive. In this contribution, we amalgamate uplink mm-Wave-based and downlink VLC-based localization. We employ quantum search algorithms for reducing the computational complexity required for achieving the optimal full-search-based performance. Regarding the uplink mm-Wave-based localization, we employ a single anchor equipped with multiple Antenna Elements (AEs) and we exploit the specular multipath components created by the room's walls. The proposed solutions outperform the state-of-the-art algorithms. Furthermore, various channel models are considered, based on real indoors mm-Wave measurements. By using VLC-based triangulation for downlink and the proposed mm-Wave-based localization algorithm for uplink, there was an average positioning error of 5.6 cm in the room considered, while requiring 261 database queries on average.**

***Index Terms*—Computational Complexity, Dürr-Høyer Algorithm, Fingerprinting, Grover's Quantum Search Algorithm, Localization, mm-Wave, Quantum Computing, Visible Light Communications**

I. Introduction

Indoor localization is the process of estimating the position of an agent in an indoor environment, based on either the transmitted uplink or the downlink signals [1]. Given a single or multiple anchors, such as Access Points (AP), a user with an unknown location in the room, has to estimate its position based on an uplink of downlink signal [2]. Accurate localization may improve the performance of diverse applications, such as beam-forming [3], where a narrow *pencil* beam may be transmitted at high carrier frequencies, hence the receiver's position should be accurately estimated. Other compelling applications include network management and security [2], or assisted living [4], where accurate localization will aid activity recognition, movement pattern discoveries and it may detect anomalies. High-precision indoor localization may be used for creating new applications, such as accurate storage information in warehouses, improving coworking efficiency in office buildings by finding which meeting room is available, or where a colleague may be found, assigning the closest downlink Visible Light Communication (VLC) transmitter to the user, as well as improving the consumer's and traveller's experience in shopping malls and airports, by arranging location-oriented goods promotions and information delivery. Indoor localization may be performed by invoking various technologies, such as wireless local area networks [2], VLC systems [5] and wireless sensor networks [6], as long as there are APs, whose positions are known.

The next generations of wireless communications are expected to subsume an increasing number of heterogeneous network architectures [7]. For example, there may be femtocells, which amalgamate the high bandwidth offered by the millimeter-Wave (mm-Wave) technology [8]–[12] for the uplink and that of the VLC systems [5], [13]–[15] for the downlink. VLC systems have been shown to perform well in localizing users indoors [5], [16]–[18], based on a combination of extracted characteristics, such as the Angle-of-Arrival (AoA) or the Received Signal Strength Indicator (RSSI), as long as their limited coverage allows it. Due to the wide-spread use of Light Emitting Diodes (LED), VLC-based techniques are promising for indoor localization. However, since the Field Of View (FOV) of the LEDs employed determine the coverage, there may be users whose presence may not be evident, when relying solely on VLC solutions.

For this reason, we believe that mm-Wave systems, which may be used for the uplink in the next-generation femtocells, may also assist in the localization of indoor users. In high-user-density scenarios, the localization load may be partitioned between the downlink VLC and the uplink mm-Wave links. Ultra WideBand (UWB) systems have often been used in the literature for performing indoors localization [1], [4], [19]–[22], mainly due to their short symbol duration, which allows a better resolution of the Time of Arrivals (ToA) relying on the MultiPath Components (MPC) in the Power Delay Profile (PDP). In other words, the Inter-Symbol Interference (ISI) is reduced, since the reception of a symbol has typically been completed before a reflected copy of it arrives at the receiver. By employing UWB systems operating at mm-Wave carrier frequencies, we may exploit the benefits

The authors are with the School of Electronics and Computer Science, University of Southampton, Southampton, SO17 1BJ, UK (email: {pb1y14, da4g11, zb2g10, hvn08r, dc2n14, sxn, lh}@ecs.soton.ac.uk).

The financial support of the European Research Council under the Advanced Fellow Grant, that of the Royal Society's Wolfson Research Merit Award and that of the Engineering and Physical Sciences Research Council under Grant EP/L018659/1 is gratefully acknowledged. The use of the IRIDIS High Performance Computing Facility at the University of Southampton is also acknowledged.

that UWB system offer in localization applications, while allowing multiple Antenna Elements (AE) to be installed at the anchors, due to their compact construction, for improving the estimation of the agents' positions. Furthermore, the high available bandwidth of the mm-Wave systems, as well as their beamforming capabilities, may also increase the system's performance, once the users have been accurately localized. As we demonstrate in this paper, the specific construction of the Antenna Array (AA), which employs multiple AEs has to be harmonized with the symmetry of the room, as well as with the location of the anchor. The UWB-based indoor localization solutions [4], [21], [22] are based on both the Line Of Sight (LOS) path, as well as on the specular MPCs of the received signal, where a single anchor equipped with a single antenna is employed. We have also adopted this approach for our investigations in mm-Wave systems.

The fingerprinting method [5] may be employed In both the VLC-based and the RF-based indoors localization categories, if high accuracy is required. The fingerprinting method assumes prior knowledge of the room's topology, which has been divided in a virtual grid. Additionally, it exploits that noiseless signals received or transmitted from the center of each virtual tile of the grid, depending on whether they correspond to downlink or uplink, respectively, are available in a pre-built database. A subset of that database is then searched based on the specific metric adopted for determining the most likely tile that the agent transmitted from. Therefore, the computational complexity of the search in the fingerprinting database may become excessive, especially when the required accuracy is high, which means that the tile-size of the virtual grid is small, hence the number of tiles is high. Motivated by achieving a high precision, we employ a Quantum Search Algorithm (QSA), namely the Dürr-Høyer Algorithm (DHA) [23], which find the minimum entry in an unsorted database having N elements, using as few as $O(\sqrt{N})$ Cost Function Evaluations (CFE). The DHA is based on Grover's QSA [24]–[26], which is one of the earliest algorithms in quantum computing and forms the basic block of various quantum algorithms. In fact, we have previously employed Grover's QSA and the DHA for diverse applications, such as multi-user detection in the uplink of Non-Orthogonal Multiple Access (NOMA) systems [27]–[31], for vector precoding in multi-user transmission in the downlink of NOMA systems [32], for joint channel estimation and data detection [33] and for multi-objective routing in self-organized networks [34], [35]. Even though the operation of Grover's QSA will in practice be prone to quantum decoherence [36], in this contribution we assume perfect operation of both the quantum circuits, as well as of the classical components.

Against this background, our novel contributions are:

1) *We conceive an indoor localization algorithm for mm-Wave communications systems in Section II, relying on a single multi-antenna-aided anchor, which exploits both the LOS as well as the specular MPCs [4], [22], based on practical indoor measurements of mm-Wave systems [37]. The proposed algorithm initially reduces the search space and subsequently optimizes the estimated position based on a fingerprinting database, which is constructed with the aid of the room's floor plan, taking into account the required localization accuracy, as well as the affordable complexity. The small wavelength of mm-Wave communications allows an anchor to use multiple antenna elements in a compact construction, which may be exploited for improving the localization estimation of the users.*
2) *We show that QSAs may be employed for reducing the computational complexity of both the mm-Wave-based and the VLC-based localization algorithms in Section IV, while retaining the optimal performance of a full search, after we have briefly introduced the VLC-based localization model of [5] in Section III.*
3) *We demonstrate the importance that the shape of the antenna array and various design parameters have on the performance of localization in Section V. In the spirit of contribution (1) and (2), we exploit the benefits of the high downlink bandwidth of VLC [5] and that of its uplink complement constituted by mm-Wave communications in Section V, where their potential collaboration may reduce both a user's estimated position deviation from its true position and the complexity of the localization. Furthermore, we argue that a potential joint optimization of the anchors' positions in the two systems is beneficial.*
4) *Throughout the paper, we have opted for presenting a step-by-step analysis and tutorial both for the proposed mm-Wave localization algorithm and for the VLC localization algorithm. Additionally, we quantify the effect of its features and parameters on the attainable localization performance and complexity.*

Tables I and II describe the parameters that will be used in the mm-Wave-based localization, while Table III describes those employed in the VLC-based localization. Due to the plethora of different symbols and parameters in this manuscript, we request the reader to refer to these tables as often as required.

II. Localization in Uplink mm-Wave Systems

Let us proceed by introducing the indoor environment that will be considered for localization in both the analysis and the simulations. Figure 1 presents a bird's eye view of a room. Assuming that the $[0, 0]$ point is at the bottom left corner of the room, let us install a multi-antenna mm-Wave anchor at the $\mathbf{a}_l^{(i)} = [a_{l,x}^{(i)}, a_{l,y}^{(i)}, a_{l,z}^{(i)}]^T$ position. In $\mathbf{a}_l^{(i)}$, the superscript (i) determines the index of the N_A physical anchors the positions refer to, where $i = 1, \ldots, N_A$, while the subscript l corresponds to the index of the Virtual Anchor (VA) of the ith physical anchor, as defined below. Hence, the position of a physical anchor has a subscript of $l = 0$. The positions of a physical anchor's VAs may be found with high precision if the floor plan of the room is available, and they correspond to the imaginary anchors that would have received a specular MPC as a LOS path. Naturally, the VAs "exist" outside this room, since in our scenario all specular MPCs are generated by the four walls. Therefore, given that the ith physical anchor is located at $\mathbf{a}_0^{(i)} = [a_{0,x}^{(i)}, a_{0,y}^{(i)}, a_{0,z}^{(i)}]^T$ in a room with floor dimensions W_x and W_y, the four VAs depicted in Fig. 1 would be located

This article has been accepted for publication in a future issue of this journal, but has not been fully edited. Content may change prior to final publication. Citation information: DOI 10.1109/ACCESS.2017.2733557, IEEE Access

TABLE I: mm-Wave System Parameters

Symbol	Description
N_A	Number of anchors
M	Number of AEs per anchor
L	Number of VAs, equal to the number of specular paths
$\mathbf{a}_l^{(i)}$	Position of the ith physical anchor's lth VA
$\mathbf{p}$	User's position
$\mathbf{r}_m^{(i)}(t)$	Received signal at the ith physical anchor's mth AE at time t
$h_l^{(i)}$	Channel state of the lth path between the user and the ith physical anchor
$a_m(\phi,\theta)$	Phase rotation at the mth AE of the AA with respect to the center of the AA, when the angles of irradiance and incidence are ϕ and θ, respectively
$s(t)$	Transmitted signal at time t
$\tau_l^{(i)}$	Time of arrival of the lth path between the user and the ith physical anchor
$\nu^{(i)}(t)$	Diffusion multipath noise at the ith physical anchor at time t
$w_m^{(i)}(t)$	AWGN at the ith physical anchor's mth AE at time t
$EIRP$	Equivalent isotropic radiated power in dBm
$PL_l^{(i)}$	Path loss of the lth path between the user and the ith physical anchor
λ	Wavelength of the transmitted signal
f_c	Carrier Frequency
c	Speed of light
$\bar{n}_l$	Path loss exponent of the lth path
$d_l^{(i)}$	Distance between the user and the lth VA of the ith physical anchor
$\chi_{l,sh}$	Shadowing coefficient of the LOS $(l=0)$ NLOS $(l>0)$ paths
$\sigma_{l,sh}$	Standard deviation of the shadowing coefficient of the lth path
BW	Bandwidth of the transmitted signal
XPD	Cross-polarization discrimination coefficient

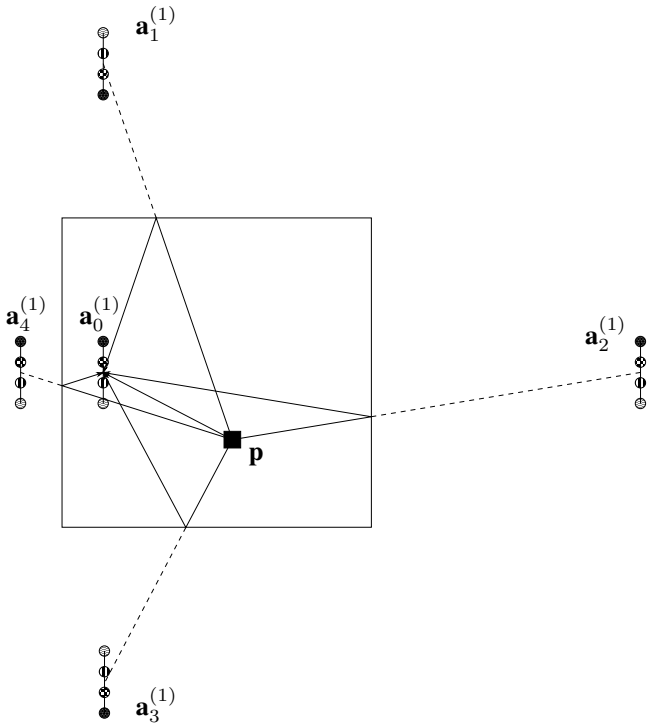

Fig. 1: Floor plan of the room, where the signal from the agent with the unknown position $\mathbf{p} = [p_x, p_y, p_z]^T = [8.25, 4.25, 0.85]^T$ (black square) is received by the four AEs (different circles) of the physical anchor's uniform linear array at $\mathbf{a}_0^{(1)} = [a_{0,x}^{(1)}, a_{0,y}^{(1)}, a_{0,z}^{(1)}]^T = [2, 7.5, 2.5]^T$ as a direct path and four specular MPCs. since the carrier frequency is $f_c = 28$ GHz, the four AEs are placed with a $\lambda/2 = 5.4$ mm spacing. The four specular MPCs may be considered as having been received by VAs, in the same fashion as distributed MIMO. Note that the AEs of the physical anchor and the VAs are mirrored.

at

$$\mathbf{a}_1^{(i)} = \left[a_{0,x}^{(i)},\, 2\cdot W_y - a_{0,y}^{(i)},\, a_{0,z}^{(i)}\right]^T \tag{1}$$

$$\mathbf{a}_2^{(i)} = \left[2\cdot W_x - a_{0,x}^{(i)},\, a_{0,y}^{(i)},\, a_{0,z}^{(i)}\right]^T \tag{2}$$

$$\mathbf{a}_3^{(i)} = \left[a_{0,x}^{(i)},\, -a_{0,y}^{(i)},\, a_{0,z}^{(i)}\right]^T \tag{3}$$

$$\mathbf{a}_4^{(i)} = \left[-a_{0,x}^{(i)},\, a_{0,y}^{(i)},\, a_{0,z}^{(i)}\right]^T \tag{4}$$

Please note that we have assumed no specular reflection arrives at the physical anchor from the floor or the ceiling, therefore only four VAs are considered. Furthermore, due to the high path loss of MPCs at mm-Wave frequencies, we have only considered the primary specular MPCs due to a single reflection, since the power received from multiple-reflection MPCs will be under the noise level. The user and the physical anchor are assumed to be synchronised. Furthermore, if the power received due to multiple reflected paths was above the noise level and they were included in the proposed localization algorithm, the resultant localization accuracy would be improved. However, more VAs should be considered, which would result in a increased computational

This article has been accepted for publication in a future issue of this journal, but has not been fully edited. Content may change prior to final publication. Citation information: DOI 10.1109/ACCESS.2017.2733557, IEEE Access

TABLE II: mm-Wave System Parameters (continued)

Symbol	Description
$\Delta t_m(\phi, \theta)$	Time difference of arrival between the mth AE and the center of the AA, when the angles of irradiance and impedence are ϕ and θ, respectively
r	Radius of the uniform circular array
β	Roll-off factor of the RRC filter
T	Symbol period
f_s	Sampling frequency
$P_{w,\,dBm}$	AWGN power in dBm
$SDNR$	Signal to Diffusion Noise Ratio
ξ	Exponential decay constant of DM noise's exponential decay process
u	Uniformly distributed random number
$y_m^{(i)}(t)$	Matched filter output at the mth AE of the ith physical anchor
$r_s(t)$	Impulse response of the raised cosine filter at time t
$z^{(i)}(t)$	Total power at the outputs of the MFs at the ith physical anchor
N_p	Maximum number of selected peaks
$N_{s,\,LOS}$	Maximum number of samples difference between the actual ToA of the LOS path and that of a tile's LOS path, for that tile to be included in the reduced-size database
$N_{s,\,NLOS}$	Maximum number of samples difference between the ToA of a tile's NLOS path and any estimated peak, for that tile to be included in the reduced-size database
N_T	Number of tiles in the room
N_{DB}	Number of tiles in the searched database
CF_{mmW}	Cost function in mm-Wave localization
$\mathbf{p}_k$	Position of the center of the kth tile
$\hat{y}_m^{(i,k)}$	Reconstructed, noiseless MF output at the mth AE of the ith physical anchor, if the signal was transmitted from the center of the kth tile

TABLE III: VLC System Parameters

Symbol	Description
N_{AP}	Number of Access Points
$P_{T_x,opt}$	Transmitted optical power of each AP
$P_{R_x}^{(n)}$	Optical power received by the user from the nth AP
$h_{LOS}^{(n)}$	LOS path between the nth AP and the user
$h_{NLOS}^{(n)}$	NLOS path between the nth AP and the user
$h_l^{(n)}$	Channel state of the nth AP's lth reflection
ψ_c	Half of user's Field-Of-View
m	Order of Lambertian emission
$\phi_{1/2}$	Semi-angle at half power
d_n	Distance between the user and the nth AP
$d_{n,l}$	Distance between the nth AP and the reflection point on the wall
$d_{l,p}$	Distance between the reflection point on the wall and the user
A_r	Physical area of the photodetector
$T_s(\psi)$	Optical filter's gain
$g(\psi)$	Optical concentrator's gain
n_{rfr}	Refraction index
ρ	Reflection efficiency of the wall's surface
A_{wall}	Wall's reflective area
α	Angle of irradiance at the reflection point
β	Angle of irradiance at the user
I_0	Center luminous intensity per LED
$N_{DB,\,VLC}$	Size of searched database
CF_{VLC}	Cost function in VLC localization

complexity. The specific PDP of the system depends on the application scenario, i.e. on the positions of both the physical anchor and the user, as well as on the dimensions of the room. The positions of the VAs depend solely on the physical anchor's position, but not on that of the agents. Therefore, only the floor plan's knowledge is required, but no prior knowledge of the users' positions is necessitated. In Fig. 1, we have employed a Uniform Linear Array (ULA) with four AEs, noting that in general different formations of the AEs offer different advantages. Therefore, it is important during the signal combining stage to take into account the fact that the AEs of the VAs' antenna arrays are at different positions, when compared to that of the physical array. More specifically, the antenna arrays of the VAs are mirrored with respect to

the four walls used for creating them. This becomes evident in Fig. 1, where we have printed each AE using a different pattern.

Let us now assume that a user, whose position has to be estimated, is at position $\mathbf{p} = [p_x, p_y, p_z]^T$, as illustrated in Fig. 1. In our systems, every user is assumed to use a single antenna and since a user has no prior knowledge of the anchor's position in the room, an omnidirectional signal is transmitted. The transmitted uplink signal arrives at the physical anchor via five paths, hence the following signal is received:

$$r_m^{(i)}(t) = \sum_{l=0}^{L} h_l^{(i)} \cdot a_m\left(\phi_l^{(i)}\right) \cdot s\left(t - \tau_l^{(i)}\right) + s(t) * \nu^{(i)}(t) + w_m^{(i)}(t), \quad (5)$$

where $r_m^{(i)}(t)$ is the signal received by the ith physical anchor's mth AE at time instant t, with $i = 1, \ldots, N_A$ and $m = 1, \ldots, M$, while $l = 0, 1, \ldots, L$ is the index of the LOS and NLOS paths arriving at the anchor, with $l = 0$ referring to the LOS path and L equal to the number of specular MPCs ($L = 4$ in our scenario). Still referring to (5), $h_l^{(i)}$ is the channel coefficient of the lth path between the user and the ith physical anchor, which in our scenario only includes the effect of the path loss. In other words, no fading channels have been assumed in our systems. The function $a_m\left(\phi_l^{(i)}\right)$ in (5) outputs the phase rotation of the signal received by the ith anchor's mth AE with respect to the signal that would have been received at the center of the antenna array (if an AE was there), based on the AoA of the signal that arrived on the lth path. In the same equation, $\tau_l^{(i)}$ is the delay experienced by the signal received by the ith physical anchor from the lth path, while $s(t)$ is the transmitted signal, which is the output of a root-raised cosine filter and it is known to both the user, as well as to the anchors. The convolution $s(t) * \nu^{(i)}(t)$ describes the Diffused Multipath (DM) noise that arrives at the physical anchors. The diffused multipath noise cannot be deterministically estimated and it models the signals received due to the diffusion that the transmitted signals experience by being scattered by non-deterministic or stationary objects in the room. The diffusion coefficient $\nu^{(i)}(t)$ is different for every physical anchor i, and the associated diffused component appears after the arrival of the direct path, as well as after each specular path and it decays exponentially with time. Finally, $w_m(t) \sim \mathcal{N}(0, N_0)$ describes the Additive White Gaussian Noise (AWGN) experienced by the ith physical anchor's mth AE, which obeys a normal distribution with zero mean and a variance of N_0.

In the following subsections, we will further investigate the elements of (5), while referring to our propagation scenario illustrated in Fig. 1.

A. Path Loss

The channel coefficient of the lth path between the user and the ith physical anchor $h_l^{(i)}$ of (5) may be described as

$$h_l^{(i)} = 10^{\left(EIRP[dBm] - PL_l^{(i)}[dB]\right)/20}, \quad (6)$$

where the Equivalent Isotropically Radiated Power (EIRP) is the product of the transmitted power and of the transmit antenna gain, while the Path Loss (PL) of the lth path received by the ith physical anchor is described in dB as

$$PL_l^{(i)}[dB] = 20 \cdot \log_{10}\left(\frac{4\pi}{\lambda}\right) + 10 \cdot \bar{n}_l \cdot \log_{10}\left(d_l^{(i)}\right) + \chi_{l,sh}. \quad (7)$$

In (7), $\lambda = c/f_c$ is the wavelength, c is the speed of light and f_c is the carrier frequency, $d_0 = 1$ m is a reference distance and $d_l^{(i)}$ is the three-dimensional distance travelled by the lth path between the user and the ith physical anchor. In (7), $\bar{n}_l$ is the PL exponent of the lth path, which depends both on the carrier frequency, as well as on whether the signal is received via a direct or a reflected path and on the particular nature of the room, where the latter is different for airports, empty warehouses and for office spaces in use. Finally, $\chi_{l,sh}$ in (7) represents the shadowing that the transmitted signal experiences for the lth path, with the shadowing coefficient having a lognormal distribution associated with $\chi_{l,sh}[dB] \sim \mathcal{N}(0, \sigma^2_{l>0,sh})$, where $\sigma^2_{l>0,sh}$ is the variance of the lognormal distribution, which also depends on the carrier frequency and on whether the signal was received via a LOS or NLOS path, as well as on the room.

In [37], the authors presented measurements performed in indoors office environments and proposed channel models for generalizing the aforementioned measurements. The path loss model described in (7) is termed as the Close-In (CI) free space reference distance model. The CI path loss model of (7) assumes that the transmit and receive antennas are co-polarized. In the scenarios, where the antennas are cross-polarized, it was proposed in [37] to include a constant attenuation factor, termed as the Cross-Polarization Discrimination (XPD), resulting in the Close-In reference distance with XPD (CIX) based PL model, as encapsulated in

$$PL_l^{(i)}[dB] = 20 \cdot \log_{10}\left(\frac{4\pi}{\lambda}\right) + 10 \cdot \bar{n}_l \cdot \log_{10}\left(d_l^{(i)}\right) + \chi_{l,sh} + XPD_l\ [dB]. \quad (8)$$

As it may be observed in (8), the XPD_l factor was found to be different for the LOS and the NLOS paths.

B. Phase Rotation at Antenna Arrays

Each AE in an AA receives the transmitted signal with a different phase with respect to the other AEs, based on the inter-element distance.

1) Uniform Linear Arrays: When a ULA of antenna elements is used, such as the one depicted in Fig. 1, and assuming that the ith physical anchor's position $\mathbf{a}_0^{(i)}$ refers to the center of the ULA, the ULA output of the mth AE is equal to [38]

$$a_m\left(\phi_l^{(i)}\right) = e^{j \cdot 2 \cdot \pi \cdot f_c \cdot \Delta t_m\left(\phi_l^{(i)}\right)}, \quad (9)$$

where $\Delta t_m\left(\phi_l^{(i)}\right)$ is the time difference between the arrival of the lth path at the center of the ith physical anchor's ULA and at the mth element of the ULA. Since the ULAs of the VAs have the same spacing between the AEs, even though their

This article has been accepted for publication in a future issue of this journal, but has not been fully edited. Content may change prior to final publication. Citation information: DOI 10.1109/ACCESS.2017.2733557, IEEE Access

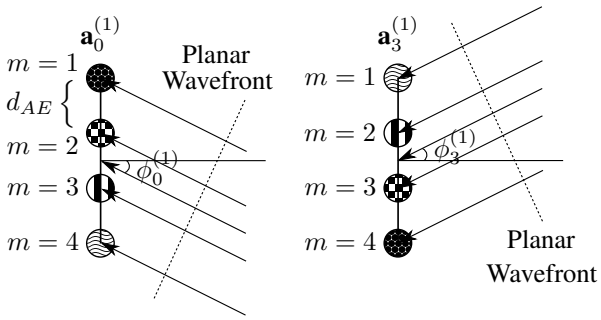

Fig. 2: The arrival of the wavefront at the ULA of the physical anchor at $\mathbf{a}_0^{(1)}$ and at the south VA at $\mathbf{a}_3^{(1)}$. Knowledge of the angle of arrival $\phi_l^{(1)}$ and of the distance between two AEs d_{AE} are sufficient for reconstructing the phase difference of the signal arriving at the center of the ULA and the AEs. Note that the indexing of the AEs is performed from top to bottom, resulting in different physical AEs having the same index, depending on the VA.

position on the ULA is mirrored with respect to the walls, let us initially investigate the phase rotation experienced by the direct path. Based on Fig. 2, when there is an even number of AEs M in the ULA, the time difference $\Delta t_m\left(\phi_l^{(i)}\right)$ between the mth AE of the ith ULA and the center of that ULA is stated in (10) (top of the next page). In (10), $m=1$ refers to the top AE and $m=M$ to the bottom AE in Fig. 2, d_{AE} is the spacing between two neighbouring AEs, $\phi_l^{(i)}$ is the AoA of the direct signal to the ith physical anchor and c is the speed of light.

The angle between the user and the physical anchor is

$$\phi_l^{(i)} = \begin{cases} \mu_l^{(i)} & p_x > a_{l,x}^{(i)} \\ \text{sign}\left(\mu_l^{(i)}\right)\cdot\pi - \mu_l^{(i)} & p_x < a_{l,x}^{(i)} \\ 0 & p_x = a_{l,x}^{(i)} \end{cases}, \tag{11}$$

where

$$\mu_l^{(i)} = \tan^{-1}\left(\frac{a_{l,y}^{(i)} - p_y}{a_{l,x}^{(i)} - p_x}\right). \tag{12}$$

As far as the VAs are concerned, the AEs of the physical anchor's ULA are reflected with respect to the VA's associated wall, and the same procedure applies for finding the AoA based on (11) and (12). Afterwards, the arrival time difference with respect to the center of the ULA is calculated based on (10) and the ULA output is found by evaluating (9). Please note that the angles calculated based on (11) are with respect to the VAs' positions.

2) Uniform Circular Arrays: We also employ Uniform Circular Arrays (UCA), since the vertical symmetry of the ULA with respect to the AoAs will cause a problem in the localization, as we will see in the following sections.

A UCA with four AEs is illustrated in Fig. 3. The UCA output is the same as that of the ULA, which is given in (9). Nonetheless, there is a difference in the calculation of the time difference between the arrival of the signal at an AE, compared to its arrival at the center of the UCA, since the

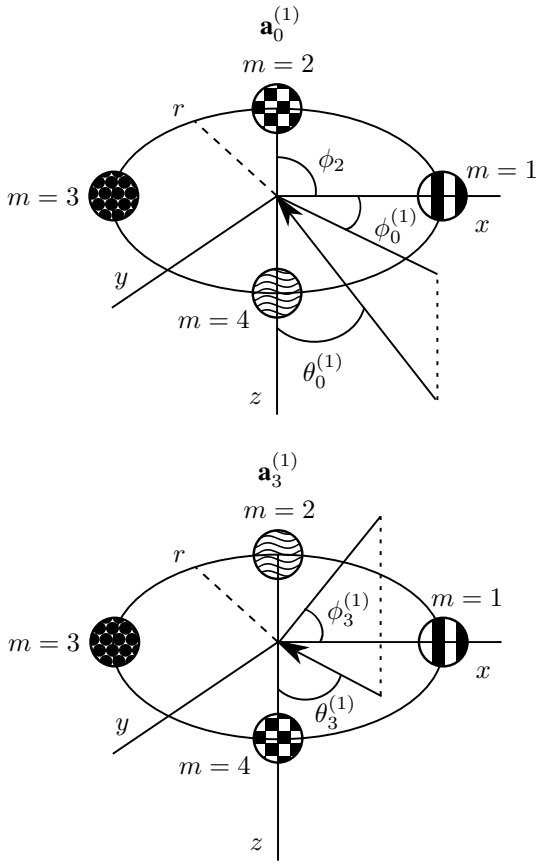

Fig. 3: Signal reception at the UCA of the physical anchor at position $\mathbf{a}_0^{(1)}$ and at the south VA at position $\mathbf{a}_3^{(1)}$. Knowledge of the azimuthan and elevation angles of arrival $\phi_l^{(1)}$ and $\theta_l^{(1)}$, as well as of the UCA's radius r and number of AEs M are sufficient for reconstructing the phase difference of the signal arriving at the center of the UCA and that which arrives at the AEs. Note that the indexing of the AEs is performed in a counter clockwise direction starting from the x axis, resulting in different physical AEs having the same index, depending on the VA.

AEs have different positions. Furthermore, both the azimuthal angle $\phi_l^{(i)}$ and the elevation angle $\theta_l^{(i)}$ affect the resultant phase difference, as exemplified in Fig. 3. More specifically, we have

$$\Delta t_m\left(\phi_l^{(i)}, \theta_l^{(i)}\right) = -\frac{r}{c}\cdot\sin\left(\theta_l^{(i)}\right)\cdot\cos\left(\phi_l^{(i)} - \phi_m\right), \tag{13}$$

where r is the radius of the UCA and ϕ_m is the angle of the mth AE with respect to the horizontal axis that passes through the center of the UCA. Please note that again, the indexing of a UCA's AE will begin counter-clockwise from the right-hand side of the horizontal axis that passes throught the UCA's center, which results in the same AE having a different index, when it belongs to a VA's UCA, due to the reflection with respect to the walls, as illustrated in Fig. 3 for the South-VA at position $\mathbf{a}_3^{(1)}$. The azimuthan angle of the mth AE is calculated as

$$\phi_m = 2\cdot\pi\cdot\frac{m-1}{M}, \quad m = 1, 2, \ldots, M. \tag{14}$$

This article has been accepted for publication in a future issue of this journal, but has not been fully edited. Content may change prior to final publication. Citation information: DOI 10.1109/ACCESS.2017.2733557, IEEE Access

$$\Delta t_m\left(\phi_l^{(i)}\right) = \begin{cases} \text{sign}\left(-\phi_l^{(i)}\right) \cdot \frac{\left[\frac{d_{AE}}{2} + \left(\frac{M}{2} - m\right) \cdot d_{AE}\right] \cdot \left|\sin\left(\phi_l^{(i)}\right)\right|}{c}, & m < \frac{M}{2} \\ \text{sign}\left(\phi_l^{(i)}\right) \cdot \frac{\left[\frac{d_{AE}}{2} + \left(m - \frac{M}{2} - 1\right) \cdot d_{AE}\right] \cdot \left|\sin\left(\phi_l^{(i)}\right)\right|}{c}, & m > \frac{M}{2} \end{cases} \tag{10}$$

The azimuthan angle between the lth received path and the UCA $\phi_l^{(i)}$ may be found as described in (11), while the elevation angle $\theta_l^{(i)}$ is calculated as in

$$\theta_l^{(i)} = \cos^{-1}\left(\frac{a_{l,z}^{(i)} - p_z}{d_l^{(i)}}\right), \tag{15}$$

where $d_l^{(i)}$ is the distance travelled by the lth path before reaching the ith physical anchor.

Please note that none of these parameters are known at the anchors, hence they cannot be exploited for finding the user's position. However, the equations may be used for reconstructing a noiseless signal as if it was transmitted from a position $\hat{\mathbf{p}}$ in order to determine how similar the received signal is to the noiseless reconstructed one. The localization algorithm will be investigated in detail in the following section, but we believe that the motivation of our analysis in this section should be made explicit. The radius of the UCA is $r = 0.3536 \cdot \lambda$, in order for the distance between two neighbouring AEs to be equal to $\lambda/2$.

C. Pulse Shaping

The user transmits a single Binary Phase Shift Keying (BPSK) modulated symbol $+1$, pulse shaped with the aid of a Root Raised Cosine (RRC) filter having a roll-off factor of β. The impulse response of the RRC, which is the transmitted signal in (5), is equal to [39]

$$s(t) = \frac{4\beta}{\pi\sqrt{T}} \frac{\cos\left(\frac{(1+\beta)\pi t}{T}\right) + T \cdot \frac{\sin\left(\frac{(1-\beta)\pi t}{T}\right)}{4\beta t}}{1 - \left(\frac{4\pi t}{T}\right)^2}, \tag{16}$$

where T is the symbol period.

At the receiver, the signal $r_m^{(i)}(t)$ of (5) received by the mth AE of the ith physical anchor passes through a matched RRC filter. Since different AEs will experience different noise contamination, the diversity provided by analyzing the summation of the received powers at the outputs of the MF operations may improve the ability to distinguish the useful signal and the AWGN.

D. Diffused Multipath

The diffused multipath noise $\nu(t)$ in (5) models the MPCs, which cannot be deterministically estimated and they are physically caused by reflections due to small or moving objects [40]–[43]. In our systems we have opted for modelling the DM noise power as an exponentially decaying process triggered by each reception of a deterministic specular MPC, including the direct path. This would result in an amplitude of [43]

$$\nu(t) = \frac{h_{l>0}^{(1)}(t)}{\sqrt{10^{SDNR/10}}} \cdot \sqrt{e^{-\frac{t}{\xi}}} \cdot e^{j \cdot 2 \cdot \pi \cdot u}, \tag{17}$$

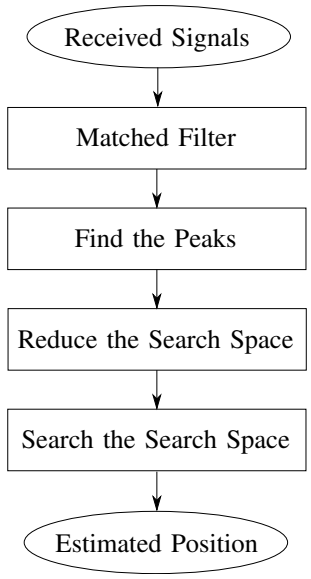

Fig. 4: Flow chart of the fingerprinting method using AAs in mm-Wave Systems.

where u is a random number obeying the uniform distribution $u \sim \mathcal{U}(0,1)$, and ξ is the exponential decay constant of the exponential decay process. Still referring to (17), we have chosen the peak power of the DM noise to be a scaled version of the power received by the specular MPC at that same time, since $h_{l>0}^{(1)}(t)$ is the channel state of a NLOS path at time t, received by the first physical anchor. By introducing in (17) the *Signal to Diffusion Noise Ratio* (SDNR), measured in dB, we are able to scale the received DM noise power in our simulations. Please note that the SDNR is assumed to be constant in time.

The resultant DM noise that arrives at the receiver is the convolution of the noise in (17) with the transmitted signal of (16) as stated in (5) and it passes through the matched RRC filter, as described in Section II-C. The DM noise is a colored noise process, in contrast to the AWGN of (5), since it does not have uniform power at all frequencies. The DM noise may degrade the accuracy of the localization process due to its random phase rotation imposed on the received signal, as stated in (17).

E. Fingerprinting using AAs in mm-Wave Systems

Let us now commence with the fingerprinting-based localization algorithm that makes use of both the AAs and of the specular MPCs. The algorithm may be divided in four processes, as illustrated in Fig. 4.

Application Scenario: After presenting each step of the algorithm, we will demonstrate it in a specific application

TABLE IV: Path Loss Parameters for $f_c = 28$ GHz

	PLE	σ_{sh} (dB)	XPD (dB)
LOS $(l = 0)$	1.1	1.8	14
NLOS $(l > 0)$	2.7	9.6	10.4

example, in order to provide deeper intuition to the process of the proposed algorithm. As an application scenario, let us consider the $15(m) \times 15(m) = 225m^2$ room seen in Fig. 1. Assuming that the $[0, 0]$ point is at the bottom left corner of the room, let us install a single $(N_A = 1)$ multi-antenna mm-Wave anchor at the position $\mathbf{a}_0^{(1)} = [2,\ 7.5,\ 2.5]^T$, which is on the ceiling close to the left wall. Since the floor plan is available, we may find the positions of the VAs that correspond to the physical anchor by finding the symmetrical positions of the physical anchor with respect to the four walls, resulting in $\mathbf{a}_1^{(1)} = [2,\ 22.5,\ 2.5]^T$, $\mathbf{a}_2^{(1)} = [28,\ 7.5,\ 2.5]^T$, $\mathbf{a}_3^{(1)} = [2,\ -7.5,\ 2.5]^T$ and $\mathbf{a}_2^{(3)} = [-2,\ 7.5,\ 2.5]^T$, as illustrated in Fig. 1. In our scenario, a user is at the unknown position $\mathbf{p} = [8.25,\ 4.25\,0.85]^T$.

The carrier frequency is set to $f_c = 28$ GHz, hence we have $\lambda \approx 1$ cm. The anchor is a ULA having $M = 4$ AEs, which have a spacing of $d_{AE} = \lambda/2 = 5$ mm, in a formation parallel to the west wall. The CIX PL model of (8) has been assumed. For a carrier frequency of $f_c = 28$ GHz as well as for a two-sided bandwidth of $BW = 800$ MHz, the authors of [37] estimated the LOS PL exponent to be equal to $\bar{n}_0 = 1.1$, while that of the NLOS paths equal to $\bar{n}_{l>0} = 2.7$. Similarly, the shadowing standard deviation was estimated as $\sigma_{0,sh} = 1.8$ dB for the direct path and $\sigma_{l>0,sh} = 9.6$ dB for the specular MPCs. Furthermore, in [37] it was estimated that $XPD_0 = 14$ dB for the direct path and $XPD_{l>0} = 10.4$ dB for the specular MPCs. The aforementioned parameters of the PL calculation for $f_c = 28$ GHz are gathered in Table IV.

The sampling frequency is equal to $f_s = 2/T = 1600$ MHz, where $T = 1/BW = 1.25$ ns is the symbol period. Regarding the noise in our scenario, an AWGN floor of $P_{w,dBm} = -174$ dBm / Hz has been included, as well as DM noise having a negative-exponential decay parameter equal to the symbol period of $\xi = T = 1/BW = 1.25$ ns. Finally, we have $SDNR = 3$ dB and the roll-off factor of the RRC filters is $\beta = 0.5$.

1) Matched Filter: As mentioned in the previous section, the signals received by each AE initially pass through an RRC MF. The output of the RRC MF at the mth AE of the ith physical anchor is

$$y_m^{(i)}(t) = \sum_{l=0}^{L} h_l^{(i)} \cdot a_m\left(\phi_l^{(i)}\right) \cdot r_s\left(t - \tau_l^{(i)}\right) + r_s(t) * \nu^{(i)}(t) + \hat{w}_m^{(i)}(t), \quad (18)$$

where $\hat{w}_m^{(i)}(t)$ is still an AWGN process with zero mean and a variance of N_0, while $r_s(t)$ is the impulse response of the raised cosine filter essentially formed by the sequential use of two root raised cosine filters, which is described as

$$r_s(t) = \text{sinc}\left(\frac{t}{T}\right) \cdot \frac{\cos\left(\frac{\pi\beta t}{T}\right)}{1 - 4\beta^2 \frac{t^2}{T^2}}. \quad (19)$$

The outputs of the MFs are then combined as encapsulated in

$$z^{(i)}(t) = \sum_{m=1}^{M} \left\| y_m^{(i)}(t) \right\|^2, \quad (20)$$

which describes the total power received by all AEs at the ith physical anchor at time instance t.

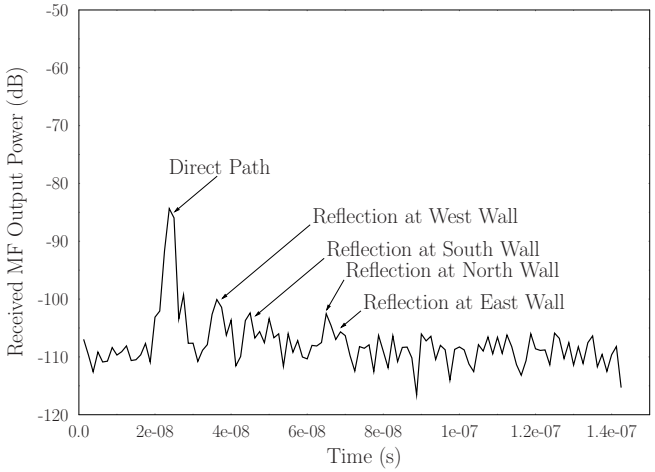

Fig. 5: Combined MF outputs at the physical anchor's ULA in the scenario of Fig. 1, when both DM and AWGN noise are included. Two matching RRC filters with $\beta = 0.5$ were used at the user and the physical anchor, while the sampling period is equal to half the symbol period.

Application Scenario: In our scenario, the combined MF output, which includes the useful signal, the DM noise and the AWGN at all AEs of the physical anchor is depicted in Fig. 5. Even though the additional power that the DM noise constitutes may not be substantial for all paths, the associated phase rotation may prove catastrophic for the success of the localization algorithm.

The combined MF output of our scenario, which is depicted in Fig. 5, was calculated based on (20). Each of the MF outputs is found based on (18). More specifically, (18) depends on the path loss of (8), the phase rotation of the ULA anchor of Section II-B1, the impulse response of the pair of RRC filters given in (19) and the diffusion multipath noise process of (17) convolved with the transmitted signal of (16).

2) Finding the Peaks: Based on the received combined power received at the output of the MF stage of Fig. 4, we may estimate the ToAs of the five paths (one direct path and four specular paths), by detecting the peaks in its PDP. Since in low-SNR scenarios some of the paths may be close ot the noise level, if we just select the specific five peaks, where the maximum received power was recorded, we may be led to wrong decisions, when peaks corresponding to noise are

This article has been accepted for publication in a future issue of this journal, but has not been fully edited. Content may change prior to final publication. Citation information: DOI 10.1109/ACCESS.2017.2733557, IEEE Access

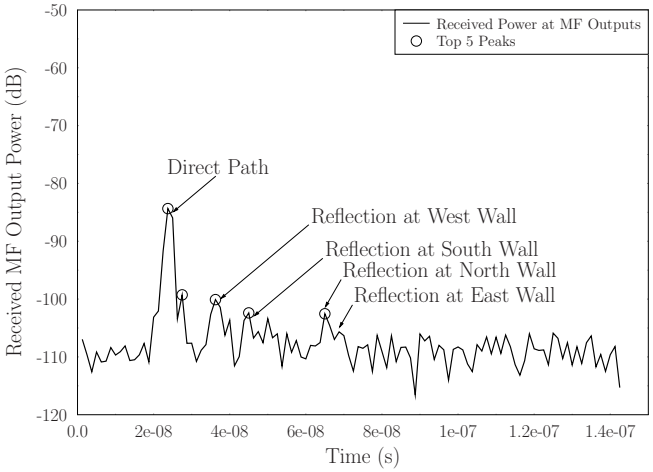

Fig. 6: The top five peaks, with respect to the received power, at the output of the MFs.

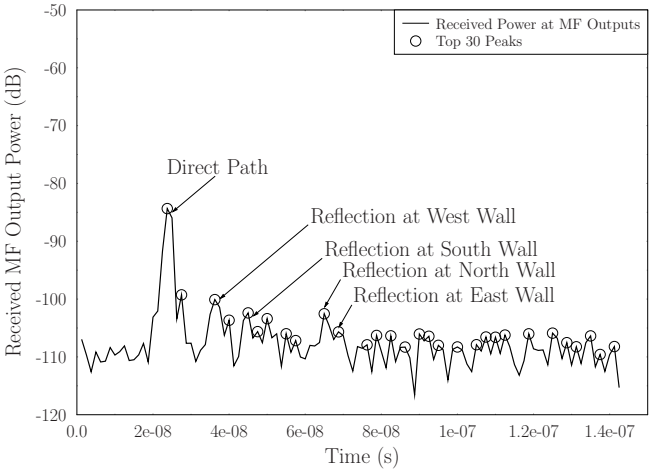

Fig. 7: The top thirty peaks, with respect to the peak persistence, at the output of the MFs.

selected. This is expected to cause issues in the next stage of Fig. 4, where the search space is shrunk, since there is a high probability that the correct position of the user would be eliminated from the search space.

In order to avoid missing the peaks that correspond to the actual received paths, we may keep the N_p number of preeminent peaks, which would be forwarded to the next stage of the algorithm. The number of peaks N_p is a design parameter and we may vary it based on the channel conditions, or on the number of VAs.

As it will be analyzed in more detail in the following stage of the algorithm, the only peak that we may identify with a confidence is the first peak that exceeds a specific power threshold, which corresponds to the direct path. Therefore, there is no need to search for peaks before the ToA of the direct path. The power threshold should take into consideration both the DM noise and the AWGN, as well as the fact that the sampling may not take place exactly at the peak of the transmitted signal. Therefore, the heuristic power threshold we used in our investigations is

$$Thr_{LOS}(t) = M \cdot h_0^{(1)} \cdot \frac{r_s\left(\frac{1}{2f_s}\right)}{2}. \tag{21}$$

The first peak, with respect to time, that is higher than the corresponding threshold value is considered to be the LOS path.

Application Scenario: In our scenario of Fig. 5, if only the top five peaks were selected, with respect to power, the second highest peak, which is caused by the DM noise, would be erroneously selected instead of the desired peak, which corresponds to the East wall's reflection, as depicted in Fig. 6. Therefore, let us set in our example $N_p = 30$, which results in finding and saving the peaks illustrated in Fig. 7.

3) Reducing the Search Space: During the shrinking stage of Fig. 4, we scan the virtual grid, generated by the fingerprinting methodology, by checking whether transmission from the center of a specific tile is capable of identifying the peaks. More specifically, transmission from the center of a tile results in the reception of five peaks at known delays, since the position of each tile in the room is known. If all these five paths match five of the peaks identified during the previous stage, then that tile is termed as a *legitimate tile* and it remains in the search space. By contrast, if no peak has been found at a specific delay, where a peak should have been found according to a specific tile, that tile is removed from the search space. Please note that the amplitude of the peak is not checked at this stage, only the ToA of each path. Please note that other techniques, such as Time Difference of Arrival (TDoA), or AoA may also be used at this stage of the algorithm, if the required infrastructure is available in order to reduce the search space.

It should be noted that even though the ToA of each path may be readily estimated from the received signals, we are not able to estimate, which specific path corresponds to which particular wall's reflection, or in other words, which path corresponds to which VA. Therefore, search spaces that are symmetric with respect to the physical anchor are expected to appear, due to the symmetry of the room considered in our scenario. Let us now define, when there is a match between the delays expected by transmitting from the center of a tile and the estimated peaks of the previous stage.

Initially, the direct path is sought, since this is the only path that is known with certainty from the MF outputs. If the expected ToA of the direct path of a tile is within $N_{s,\,LOS}$ samples from the ToA of the actually received direct path, then it is considered a match. Similarly, if there is at least one estimated peak within $N_{s,\,NLOS}$ samples from the ToA of a specular path of a tile, then it is also considered a match. Please note that all the expected ToAs of a tile should have a match in the estimated peak-database, while $N_{s,\,LOS}$ and $N_{s,\,NLOS}$ may differ. The reason that $N_{s,\,LOS}$ and $N_{s,\,NLOS}$ are greater than zero is that due to DM noise and AWGN, as well as due to the sampling times, the true peak due to a specific path may not result in an observable peak, when the

This article has been accepted for publication in a future issue of this journal, but has not been fully edited. Content may change prior to final publication. Citation information: DOI 10.1109/ACCESS.2017.2733557, IEEE Access

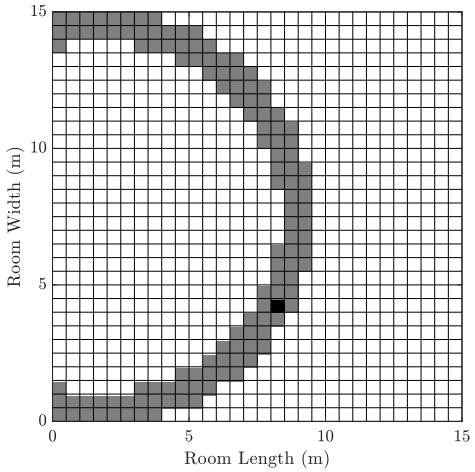

Fig. 8: The search space after the shrinking stage, where the tile size is $(0.5\,m \times 0.5\,m)$ and hence $N_T = 900$ tiles are considered, with $N_{s,\,LOS} = 1$ and $N_{s,\,NLOS} = 3$. The $N_{DB,\,mmW} = 126$ tiles included in the search space are plotted with gray color. The correct tile, which includes the true position of the user, is shown with black color. The tiles that are not included in the search space are illustrated with white color.

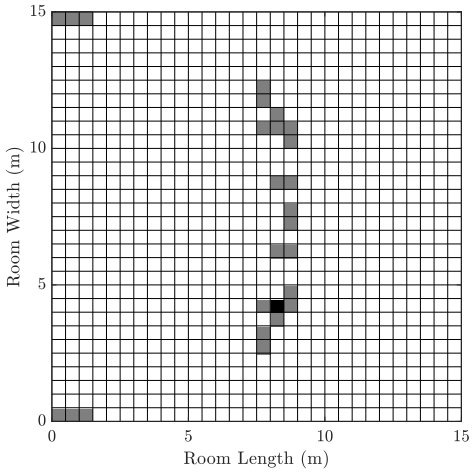

Fig. 9: The search space after the shrinking stage, where the tile size is $(0.5\,m \times 0.5\,m)$ and hence $N_T = 900$ tiles are considered, with $N_{s,\,LOS} = 1$ and $N_{s,\,NLOS} = 1$. The $N_{DB,\,mmW} = 26$ tiles included in the search space are plotted with gray color. The correct tile, which includes the true position of the user, is shown with black color. The tiles that are not included in the search space are illustrated with white color.

signals are received. In that case, if $N_{s,\,LOS}$ and $N_{s,\,NLOS}$ were equal to zero, the correct tile would not even be included in the reduced-size database. However, the above-mentioned observed peak will not have moved far away from the true peak. The reason that $N_{s,\,LOS}$ and $N_{s,\,NLOS}$ may be different is due to design considerations, where we may want the match of the direct path to be stricter than that of the specular paths.

The objective of the shrinking stage of Fig. 4 is to reduce the size of the search space, so that the complexity of the actual search, which takes place in the following stage of Fig. 4, becomes lower. Naturally, the performance will not be improved by shrinking the search space. On the contrary, if the shrinking procedure is not performed carefully, the localization performance may degrade. Therefore, the current stage describes a performance versus complexity trade-off in the localization algorithm.

Application Scenario: Figure 8 depicts the reduced search space in our scenario, when the tile size of the grid is $(0.5\,m \times 0.5\,m)$, resulting in $N_T = 900$ tiles in the room and when we have opted for $N_{s,\,LOS} = 1$ and $N_{s,\,NLOS} = 3$ samples.

The resultant search space consists of $N_{DB,\,mmW} = 126$ tiles, which constitutes the database that will be searched. The peaks found in Fig. 7 have been used for shrinking the search space. We may observe that the distance estimated by the ToA of the direct path determines the shape of the search space. If we used $N_{s,\,LOS} = 1$ and $N_{s,\,NLOS} = 1$ instead, the resultant search space would only include $N_{DB,\,mmW} = 26$ tiles, as illustrated in Fig. 9. As expected, the lower the values of $N_{s,\,LOS}$ and $N_{s,\,NLOS}$ are, the stricter the eligibility of a tile is judged and hence the smaller the shrunk search space becomes. However, this comes at the risk of excluding the correct tile from the resultant search space, due to the noise imposed on the received signals.

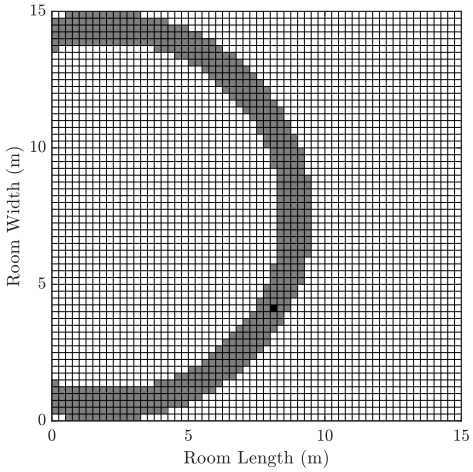

Fig. 10: The search space after the shrinking stage, where the tile size is $(0.25\,m \times 0.25\,m)$ and hence $N_T = 3600$ tiles are considered, with $N_{s,\,LOS} = 1$ and $N_{s,\,NLOS} = 3$. The $N_{DB,\,mmW} = 484$ tiles included in the search space are plotted with gray color. The correct tile, which includes the true position of the user, is shown with black color. The tiles that are not included in the search space are illustrated with white color.

Moreover, if the virtual grid was separated into $N_T = 3600$ tiles of size $(0.25\,m \times 0.25\,m)$ each, then the resultant search space would be the one shown in Fig. 10, where we have $N_{s,\,LOS} = 1$ and $N_{s,\,NLOS} = 3$ and the estimated peaks of

This article has been accepted for publication in a future issue of this journal, but has not been fully edited. Content may change prior to final publication. Citation information: DOI 10.1109/ACCESS.2017.2733557, IEEE Access

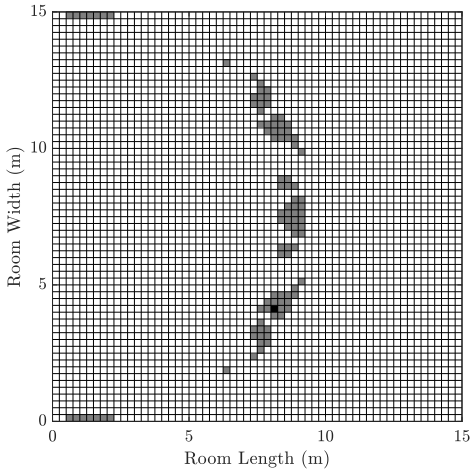

Fig. 11: The search space after the shrinking stage, where the tile size is $(0.25\,m \times 0.25\,m)$ and hence $N_T = 3600$ tiles are considered, with $N_{s,\,LOS} = 1$ and $N_{s,\,NLOS} = 1$. The $N_{DB,\,mmW} = 100$ tiles included in the search space are plotted with gray color. The correct tile, which includes the true position of the user, is shown with black color. The tiles that are not included in the search space are illustrated with white color.

Fig. 7 were used. By using a smaller tile size, the precision of the localization will be increased, but at the cost of increased complexity, since $N_{DB,\,mmW} = 484$ tiles would have to be searched in contrast to the $N_{DB,\,mmW} = 126$ tiles in the case, where each tile had a size of $(0.5\,m \times 0.5\,m)$. By changing the design parameter of $N_{s,\,NLOS} = 1$, the search space is reduced even further, as shown in Fig. 11, but the algorithm becomes more sensitive to noise. By comparing Fig. 9 and Fig. 11, which use the same design parameters of $N_{s,\,LOS} = 1$ and $N_{s,\,NLOS} = 1$, but different tile sizes, we may observe that when the tile size is smaller, more tiles are included in the resultant search space. Therefore, based on both the available complexity budget and on the target localization precision, the tile size and the design parameters $N_{s,\,LOS}$ and $N_{s,\,NLOS}$ may be tuned accordingly.

4) Exploring the Search Space: This stage of Fig. 4 determines, which particular tile in the resultant database is the most likely to include the true position of the user. In order to achieve that the noiseless received signals, which would have been received at the outputs of the RRC MFs, if the signal was transmitted from the kth tile are compared to the actual outputs of the MF of each AE according to the Cost Function (CF), of

$$CF_{mmW}(\mathbf{p}_k) = \sum_{i=1}^{I}\sum_{p=1}^{N_p}\sum_{m=1}^{M} \frac{\left\| y_m^{(i)}(t_p) - \hat{y}_m^{(i,k)}(t_p) \right\|^2}{N_i N_p M}, \quad (22)$$

where $\mathbf{p}_k = [p_{k,x},\, p_{k,y},\, p_{k,z}]^T$ is the center position of the kth tile, N_A is the number of physical anchors in the systems, N_p is the number of peaks estimated by the"Finding the peaks" stage of Fig. 4, M is the number of AEs installed at each physical anchor, t_p is the pth peak's time of arrival, and $\hat{y}_m^{(i,k)}(t_p)$ is the noiseless version of (18), if the transmitted signal had originated from the center of the kth tile, as formulated in

$$\hat{y}_m^{(i,k)}(t) = \sum_{l=0}^{L} h_l^{(i,k)} \cdot a_m\left(\phi_l^{(i,k)}\right) \cdot r_s\left(t - \tau_l^{(i,k)}\right), \quad (23)$$

where $h_l^{(i,k)}$ is the channel state, which may be reconstructed based on

$$h_l^{(i,k)} = 10^{\left(EIRP[dBm] - PL_l^{(i,k)}[dB]\right)/20}, \quad (24)$$

where $PL_l^{(i,k)}$ is based on (7) or (8), with the difference that $d_l^{(i,k)}$ is substituted in those equations, determining the distance between the ith physical anchor and the kth tile, as in

$$d_l^{(i,k)} = \left\| \mathbf{a}_l^{(i)} - \mathbf{p}_k \right\|. \quad (25)$$

Still referring to (23), $\phi_l^{(i,k)}$ is the AoA of the lth path between the ith physical anchor as well as the kth tile and it is calculated according to (11), where $\mu_l^{(i)}$ is replaced by $\mu_l^{(i,k)}$, which in turn is described by

$$\mu_l^{(i,k)} = \tan^{-1}\left(\frac{a_{l,y}^{(i)} - p_{k,y}}{a_{l,x}^{(i)} - p_{k,x}}\right). \quad (26)$$

Finally, $\tau_l^{(i,k)}$ describes the delay of the lth path between the ith physical anchor and the kth tile, and it is calculated as in

$$\tau_l^{(i,k)} = \frac{d_l^{(i,k)}}{c}, \quad (27)$$

where $d_l^{(i,k)}$ is given in (25) and c is the speed of light.

Therefore, it may be concluded that the cost function in (22) is a function of the position of a tile's center. Hence, the optimal tile, with respect to its center being the closest to the user's true position, is the one that minimizes the cost function of (22). In other words, the user's estimated position is the center of the tile that minimizes (22), as encapsulated in

$$\hat{\mathbf{p}}_{mmW} = \arg\min_{\tilde{\mathbf{p}}} CF_{mmW}(\tilde{\mathbf{p}}). \quad (28)$$

A full search of all tiles would result in an excessive search. By reducing the search space according to the previous stage's procedure, the complexity is reduced, but a high complexity may still be required.

The reason we opted for the CF of (22) is that by comparing all N_p peaks that were estimated in the corresponding stage of the algorithm, we ensure that all five peaks, which were originated by the different paths of the received signals are taken into consideration. The remaining peaks, which appear due to the DM noise, as well as to the AWGN, will inevitably increase the CF value. Therefore, a tile whose power delay profile matches the more dominant peaks, will be associated with a lower CF value. Finally, the computational complexity of the mm-Wave localization algorithm may be quantified by the number of CFEs of (22). Therefore, the full search would require $\mathcal{C}_{mmW} = N_{DB,\,mmW}$ CFEs, where $N_{DB,\,mmW} <$

This article has been accepted for publication in a future issue of this journal, but has not been fully edited. Content may change prior to final publication. Citation information: DOI 10.1109/ACCESS.2017.2733557, IEEE Access

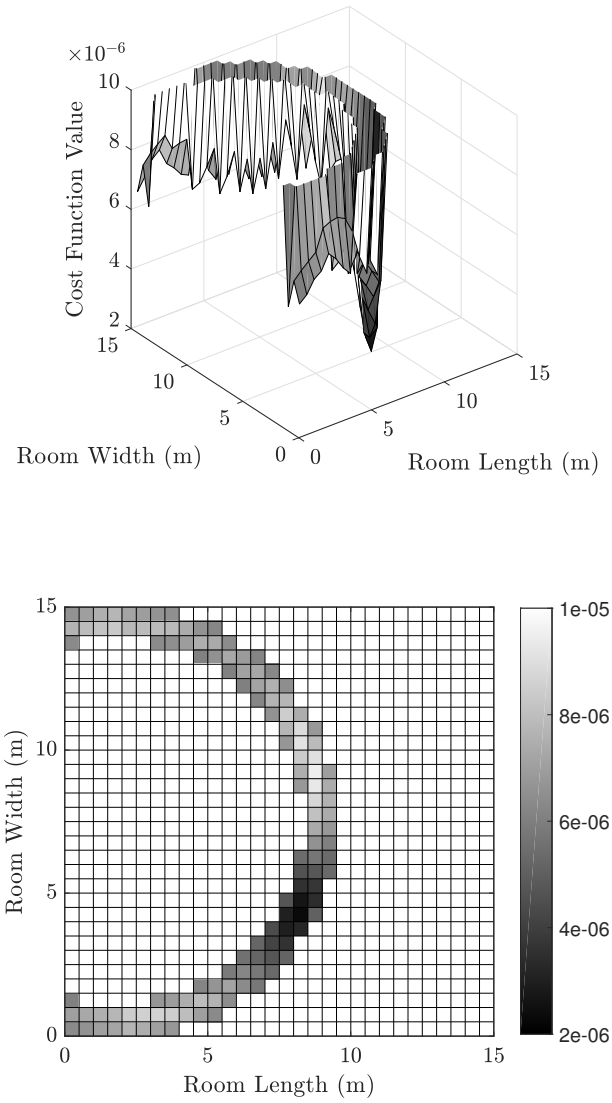

Fig. 12: The CF values of the reduced search space, where $N_{DB,\,mmW} = 126$ tiles participate, with $N_{s,\,LOS} = 1$ and $N_{s,\,NLOS} = 1$. The tile positioned at $\hat{\mathbf{p}}_{mmW} = [8.25,\, 4.25]^T$ exhibits the minimum CF value of (22) and it perfectly matches the user's position $\mathbf{p} = [8.25,\, 4.25]^T$.

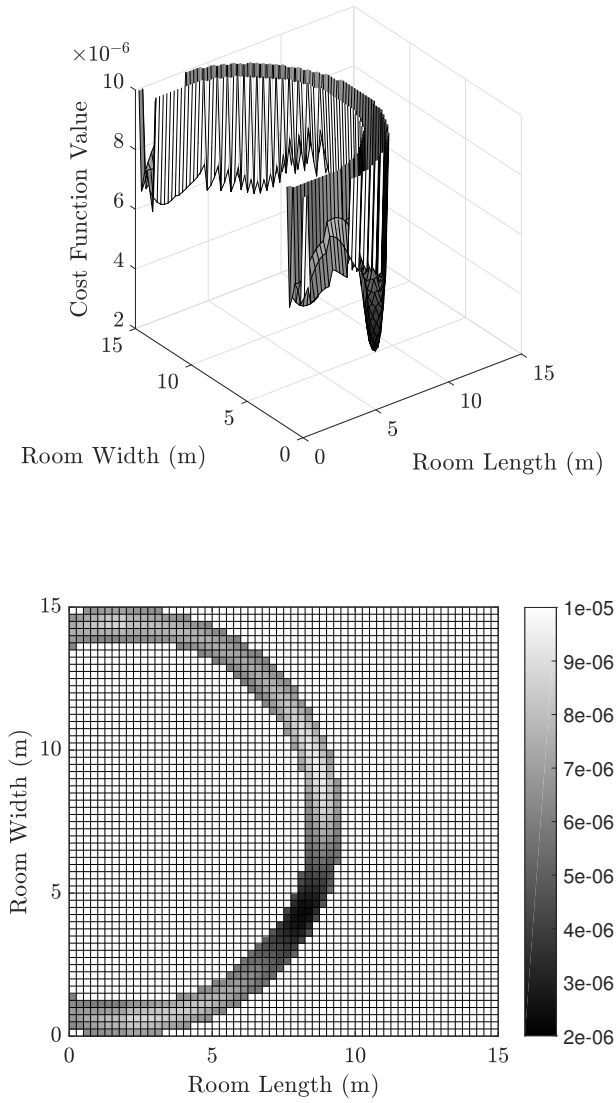

Fig. 13: The CF values of the reduced search space, where $N_{DB,\,mmW} = 484$ tiles participate, with $N_{s,\,LOS} = 1$ and $N_{s,\,NLOS} = 1$. The tile positioned at $\hat{\mathbf{p}}_{mmW} = [8.125,\, 4.375]^T$ exhibits the minimum CF value of (22) and it is 0.18 m away from the user's position $\mathbf{p} = [8.25,\, 4.25]^T$, due to the grid's quantization.

N_T due to the reduction of the search space during the corresponding stage of Fig. 4.

Application Scenario: In our scenario, when the tile size is $(0.5\,m \times 0.5\,m)$ and the design parameters are $N_p = 30$, $N_{s,\,LOS} = 1$ and $N_{s,\,NLOS} = 3$, we have a database size of 126 tiles, as illustrated in Fig. 8. The cost function values of each legitimate tile are depicted in Fig. 12. As expected, the specific tiles which are close to the user's true position $\mathbf{p} = [8.25,\, 4.25]$ have a lower CF value, while the tile located at position $\tilde{\mathbf{p}} = [8.25,\, 4.25]^T$ has the minimum CF value of $2.32 \cdot 10^{-6}$. Therefore, a full search would correctly estimate the user's position. If the tile size is $(0.25\,m \times 0.25\,m)$, again with $N_{s,\,LOS} = 1$ and $N_{s,\,NLOS} = 3$, the resultant CF values of the 484 tiles of Fig. 10 are illustrated in Fig. 13. The best estimated position after a full search is $\hat{\mathbf{p}} = [8.125,\, 4.375]^T$, which is 0.18 m away from the user's true position, due to the quantization of the grid. In general, since a user will be allowed to occupy any position in the room, smaller tiles will result in an improved average precision, as we will

This article has been accepted for publication in a future issue of this journal, but has not been fully edited. Content may change prior to final publication. Citation information: DOI 10.1109/ACCESS.2017.2733557, IEEE Access

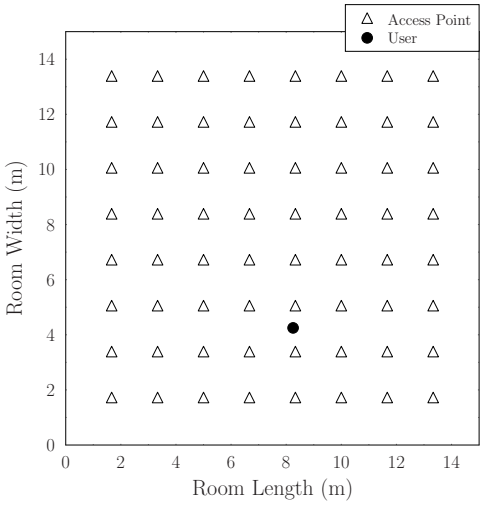

Fig. 14: Floor plan of the room, where the $N_{AP} = 8 \times 8 = 64$ APs transmit to the user at the unknown position $\mathbf{p} = [8.25,\ 4.25,\ 2.5]^T$.

demonstrate in the following sections. Since in our scenario the user's true position is exactly the same as the center of a tile of size $(0.5\,m \times 0.5\,m)$, the positioning error is zero.

III. Localization in Downlink Visible Light Communication Systems

Let us now try to localize the same user of our scenario in Section II with the aid of a downlink VLC system. In our downlink scenario, N_{AP} APs, or physical anchors, are installed close to the ceiling of the room, as illustrated in Fig. 14. The APs may be considered as LEDs that are also used to illuminate the room. The user is located at the unknown position $\mathbf{p} = [p_x,\ p_y,\ p_z]^T$ as in the uplink mm-Wave scenario. Multiple localization methodologies designed for VLC systems have been investigated in great detail in [5]. In this paper we will use the fingerprinting methodology described in [5]. Since we will not introduce additional novelty in the localization algorithm of a downlink VLC system, but rather only in the search algorithm that will be employed, the analysis in this section will focus on presenting the holistic picture of the VLC downlink and it will not be as detailed as that of the uplink mm-Wave system of the previous section. The motivated reader may refer to [5] for a tutorial-paced description of this downlink VLC localization algorithm.

The main concept of the downlink VLC localization algorithm, when the fingerprinting methodology is adopted is to determine, which specific tile would have the most similar power received by each of the N_{AP} APs. As in [5], this means that the APs are assumed to transmit in an orthogonal manner with respect to each other, so that the user can distinguish the received power levels that correspond to each individual AP. In order to relate it to the uplink mm-Wave localization algorithm, the N_{AP} APs may be related to the N_p number of peaks that were estimated during the "Finding the Peaks" stage of Fig. 4, which are naturally separated from each other in the time domain. Since the user receives a different power level from each AP, there are N_{AP} power samples for estimating that user's position.

Let us commence by defining the RSSI at the user's position, when transmitting from the nth AP, $n = 1, 2, \ldots, N_{AP}$, as [5]

$$P_{R_x}^{(n)}(\mathbf{p}) = \left(h_{LOS}^{(n)}(\mathbf{p}) + h_{NLOS}^{(n)}(\mathbf{p})\right) \cdot P_{T_x,\,opt}, \tag{29}$$

where $P_{T_x,\,opt}$ is the transmitted optical power of each AP, $h_{LOS}^{(n)}$ is the LOS path between the nth AP and the user, while $h_{NLOS}^{(n)}$ is a NLOS path between the nth AP and the user, originated by reflections from the four walls. Naturally, the transmitted light will be received by the users via multiple NLOS paths due to the multiple reflections, but as in the case of the mm-Wave model and localization algorithm of Section II, we will only consider the deterministic reflections from the four walls, which are also the most dominant NLOS paths.

In more detail, the LOS VLC channel coefficient may be described as [5]

$$h_{LOS}^{(n)}(\mathbf{p}) = \frac{(m+1)\cdot A_r}{2\cdot\pi\cdot d_n^2} \cdot \cos^m(\phi) \cdot T_s(\psi) \cdot g(\psi) \cdot \cos(\psi), \tag{30}$$

where ψ is the angle of incidence, with $0 \leq \psi \leq \psi_c$, where ψ_c is half of the user's FOV. Moreover, ϕ is the angle of irradiance, m is the order of Lambertian emission, which is described as $m = \ln(2)/\ln\left[\cos\left(\phi_{1/2}\right)\right]$, where $\phi_{1/2}$ is the semi-angle at half power, and d_n is the distance between the user and the nth AP. Still referring to (30), A_r is the physical area of a photodetector, $T_s(\psi)$ is the optical filter's gain and $g(\psi)$ is the optical concentrator's gain, which is given by $g(\psi) = n_{rfr}^2/\sin^2(\psi_c)$, where n_{rfr} is the refractive index.

The total power received due to all NLOS paths is a fraction of the transmitted optical power, as encapsulated in

$$h_{NLOS}^{(n)}(\mathbf{p}) = \sum_{l=1}^{L} h_l^{(n)}(\mathbf{p}), \tag{31}$$

where $h_l^{(n)}(\mathbf{p})$ is the channel response of the lth reflection, which is modeled as

$$h_l^{(n)}(\mathbf{p}) = \frac{(m+1)\cdot A_r}{2\cdot\pi^2\cdot d_{n,l}^2\cdot d_{l,p}^2} \cdot \rho \cdot A_{wall} \cdot \cos^m(\phi) \cdot \cos(\alpha) \cdot \cos(\beta) \cdot T_s(\psi) \cdot g(\psi) \cdot \cos(\psi), \tag{32}$$

where $d_{n,l}$ is the distance between the nth AP and the point on the specific wall that reflected the lth NLOS path, $d_{l,p}$ is the distance between that same point on the wall and the user, who is at position $\mathbf{p}$, ρ is the reflection efficiency of the wall's surface, A_{wall} is the reflective area, α is the angle of irradiance at the reflection point and β is the angle of irradiance at the user. In our scenarios, we assume a reflection efficiency of $\rho = 0.75$ and once again, (32) is valid when the angle of incidence is within half of the user's FOV ψ_c.

A. Fingerprinting-Based Localization

The fingerprinting-based localization algorithm partitions the room into a grid of N_T tiles, the potential RSS at the

This article has been accepted for publication in a future issue of this journal, but has not been fully edited. Content may change prior to final publication. Citation information: DOI 10.1109/ACCESS.2017.2733557, IEEE Access

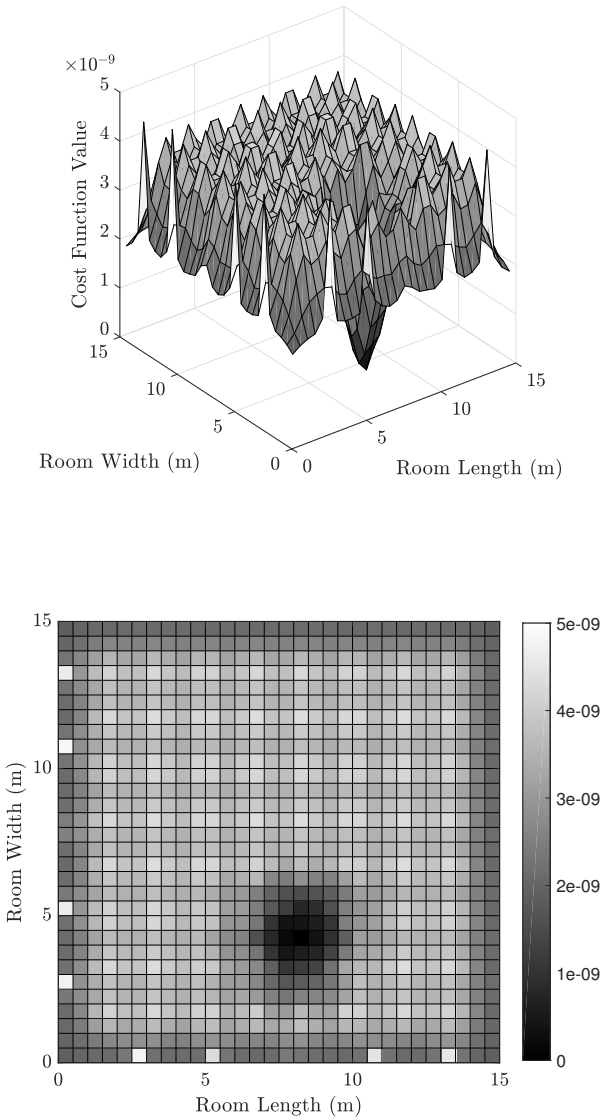

Fig. 15: The CF values of the search space in the VLC fingerprinting localization algorithm, where all $N_{DB,VLC} = 900$ tiles participate. The tile positioned at $\hat{\mathbf{p}}_{VLC} = [8.25,\ 4.25]^T$ exhibits the minimum CF value of (34) and it perfectly matches the user's position $\mathbf{p} = [8.25,\ 4.25]^T$.

center of which has already been calculated and is stored in a database. Since all tiles participate in the search, the size of the resultant database is $N_{DB,VLC} = N_T$. The calculation of the RSS at the center of the kth tile, $k = 1, 2, \ldots, N_{DB,VLC}$, is based on (29), where the unknown position of the user $\mathbf{p}$ is now replaced by the known position of the center of the kth tile $\mathbf{p}_k$, as encapsulated in

$$P_{R_x}^{(n)}(\mathbf{p}_k) = \left(h_{LOS}^{(n)}(\mathbf{p}_k) + h_{NLOS}^{(n)}(\mathbf{p}_k)\right) \cdot P_{T_x,\,opt}. \quad (33)$$

Similarly, (30), (31), and (32) are used in conjunction with $\mathbf{p}_k$. During the localization process, the actual RSS of (29) is compared to that of (33) for all tiles. The tile center which has the closest RSS value to that of the actual one is selected as the user's estimated position. This may be described according to the following CF

$$CF_{VLC}(\mathbf{p}_k) = \sum_{n=1}^{N_{AP}} \left\| P_{R_x}^{(n)}(\mathbf{p}) - P_{R_x}^{(n)}(\mathbf{p}_k) \right\|^2. \quad (34)$$

Therefore, similarly to (28), the user's estimated position is

$$\hat{\mathbf{p}}_{VLC} = \arg\min_{\tilde{\mathbf{p}}} CF_{VLC}(\tilde{\mathbf{p}}). \quad (35)$$

Application Scenario: Let us consider a scenario based on Fig. 14, where the user is positioned at $\mathbf{p} = [8.25,\ 4.25,\ 0.85]^T$ and there are $N_{AP} = 8 \times 8 = 64$ APs at a height 2.5 m from the floor, at the positions depicted in Fig. 14. Each AP consists of $60 \times 60 = 3600$ LEDs [44]. Each LED has an optical power of 5.55 mW. Therefore, the transmitted optical power of each AP in our scenario is equal to $P_{T_x,opt} = 3600 \cdot 5.55 \cdot 10^{-3} = 20$ W. The semi-angle at half power is $\phi_{1/2} = 60^o$ and the FOV is 100^o. Furthermore, the physical area of the user's photodetector is $A_r = 1$ cm^2, the optical filter's gain is $T_s(\psi) = 1$ and the refractive index is $n_{rfr} = 1.5$.

The CF values of our scenario are illustrated in Fig. 15. We may observe that the tile with center $\hat{\mathbf{p}}_{VLC} = [8.25,\ 4.25,\ 0.25]^T$ exhibits the minimum CF value of $CF_{VLC}(\mathbf{p}_k) = 0$, since it perfectly matches the true position and only deterministic contributions to the RSS have been considered. The complexity of the full search in this scenario is $N_{DB,VLC} = 900$ CFEs relying on (34).

IV. Quantum Search Algorithms in Localization

In this section rudimentary familiarity with quantum information processing is assumed. For the associated basics please refer to [45]–[47], but below we provide a brief introduction to the required basics. In quantum computing, the basic unit of information is the quantum bit, or *qubit*, which can be found in the quantum states $|0\rangle$ or $|1\rangle$, or any superposition of the two, as in

$$|q\rangle = a|0\rangle + b|1\rangle, \quad (36)$$

where $|a|^2$ and $|b|^2$ are the probabilities of obtaining the quantum states $|0\rangle$ or $|1\rangle$, when we *measure* or observe the qubit $|q\rangle$ of (36), while $a, b \in \mathbb{C}$. When a measurement or observation takes place, the superposition of states will collapse to the measured state of the classic domain. When using multiple qubits, quantum registers may be created, essentially increasing the number of legitimate quantum states exponentially. By applying quantum operators or quantum gates to the qubits, we are able to change, or evolve, their state. Furthermore, when a quantum state of two or more qubits cannot be described separately by its qubits' states, then it is said to be *entangled*. For example, let the following two qubits be in the state

$$|x\rangle = |q_1\rangle|q_2\rangle = a|00\rangle + b|11\rangle. \quad (37)$$

If it was possible to describe the state $|x\rangle$ using the individual states of the two qubits $|q_1\rangle$ and $|q_2\rangle$, then we would have

$$\begin{aligned}|x\rangle &= |q_1\rangle|q_2\rangle = (a_1|0\rangle + b_1|1\rangle)(a_2|0\rangle + b_2|1\rangle) \\ &= a_1a_2|00\rangle + a_1b_2|01\rangle + b_1a_2|10\rangle + b_1b_2|11\rangle. \end{aligned} \quad (38)$$

However, since either a_1 or b_2 should be equal to 0, based on (37), this means that (38) cannot describe (37). Therefore, (37) describes an entangled state. For an extended tutorial on quantum computing and QSAs, the motivated reader might also like to consult [27].

A. Grover's Quantum Search Algorithm

QSAs exploit these postulates of quantum computing for finding the position of an element in a database. Grover's QSA finds the index of an entry δ in a database of size N with $\sim 100\%$ probability of success, by only requiring $O(\sqrt{N})$ queries to the database. However, in order to achieve this, the desired entry δ, the size of the database N and the number of times that δ appears in the database S have to be known prior to Grover's search. From a high-level perspective, Grover's QSA [24], [25] is initialized by having an equiprobable superposition of all N legitimate quantum states, where each quantum state corresponds to the index of a single entry in the database. Therefore, $\log_2(N)$ qubits are required in order to index all N legitimate states. The goal is then to apply a specific quantum circuit L_{opt} number of times, so that when we measure the resultant state of the quantum register, the quantum state that corresponds to the index of the desired entry in the database is obtained. This is achieved by the activation of the appropriate quantum gates in Grover's quantum circuit, which change the amplitudes of the quantum register's state, so that eventually the quantum state that corresponds to the desired entry in the database has a probability to be observed close to 100%. The number of *iterations* of Grover's quantum circuit, or Grover's quantum operator, L_{opt} is equal to [24], [25]

$$L_{opt} = \left\lfloor \frac{\pi}{4}\sqrt{\frac{N}{S}} \right\rfloor. \quad (39)$$

Naturally, Grover's QSA shines in unsorted databases.

The most important quantum gate employed in Grover's quantum circuit is the *Oracle*, which is capable of querying all entries in the database simultaneously in parallel, with the aid of the superimposed qubits and a few auxiliary ones. The Oracle only manipulates the specific quantum states that correspond to the indices of those particular entries in the database, which contain δ, while leaving the rest of the quantum states unaltered. Therefore, the Oracle is tasked with *marking* the so-called solutions of the search.

B. Boyer - Brassard - Høyer - Tapp Quantum Search Algorithm

When, however, the number of occurrences S of a desired entry δ in a database of length N is not known prior to the search, and only δ and N are known, then Grover's QSA is not applicable, because according to (39) it will not be possible to determine the optimal number of Grover iterations L_{opt}. To circumvent this limitation, Boyer, Brassard, Høyer and Tapp (BBHT) proposed the BBHT QSA [26] for such search problems by relying on Grover's QSA. Again, from a bird's eye perspective, since the number of *solutions* S is not known and we are unable to determine how many times Grover's quantum circuit should be applied to the initially equiprobable superposition of states, the BBHT QSA pseudo-randomly chooses the number of Grover iterations. Even though it is highly likely that the state observed is not the desired one after the first few trials, a fact that can be checked by classically querying the database with the obtained state, the BBHT QSA has been formally proven to obtain the desired state, provided that it exists, after at most $4.5\sqrt{N/S}$ database queries. Since S is unknown, the algorithm can be terminated after $4.5\sqrt{N}$ Grover iterations, which is the highest-complexity scenario of $S = 1$. In other words, the BBHT QSA invokes Grover's QSA multiple times for a different number of Grover iterations, until the index of the desired entry is acquired. The probability of success remains at $\sim 100\%$, as in Grover's QSA.

Since the BBHT QSA is a probabilistic algorithm, its complexity may vary even between different search instances in the same database. However, even though the maximum required complexity is $4.5\sqrt{N/S}$, before we manually terminate the algorithm and conclude that there is no solution to this the search problem, when at least one solution exists, the maximum actually encountered and recorded complexity is usually much lower than $4.5\sqrt{N/S}$.

C. Dürr - Høyer Algorithm

Naturally, when the goal of a search is to find the minimum entry in an unsorted database, then δ is also unknown prior to the search. Therefore, neither Grover's nor the BBHT QSA are able to find that minimum entry, since they both require *a priori* knowledge of δ. The Dürr-Høyer Algorithm manages to find the index of the minimum entry in a database of size N with $\sim 100\%$ success probability after at least $4.5\sqrt{N}$ and at most $22.5\sqrt{N}$ database queries. In [28], we showed that the complexity of the DHA may be further reduced without sacrificing the success probability, provided that appropriate search statistics about the database are available.

Initially, the DHA randomly chooses one of the entries of the database. If there is a way of selecting an entry, the value of which is closer to the minimum one in the database, the complexity of the DHA is further reduced [28]. For example, in the signal detection field, if a low-complexity Minimum Mean Square Error (MMSE) detector is employed before the DHA, then the output of the MMSE detector may be used as the initial input to the DHA for reducing its complexity [28], [31]. After the initial input entry to the DHA δ has been selected, the BBHT QSA is employed, as described in Section IV-B, but with the difference that the Oracle now marks as solutions all the quantum states that correspond to the specific indices of those entries in the database that are smaller than δ. Naturally, there will be multiple entries in the database that have a lower value than δ. Since it is impossible to know the exact numbers of entries that are smaller than δ prior to the

This article has been accepted for publication in a future issue of this journal, but has not been fully edited. Content may change prior to final publication. Citation information: DOI 10.1109/ACCESS.2017.2733557, IEEE Access

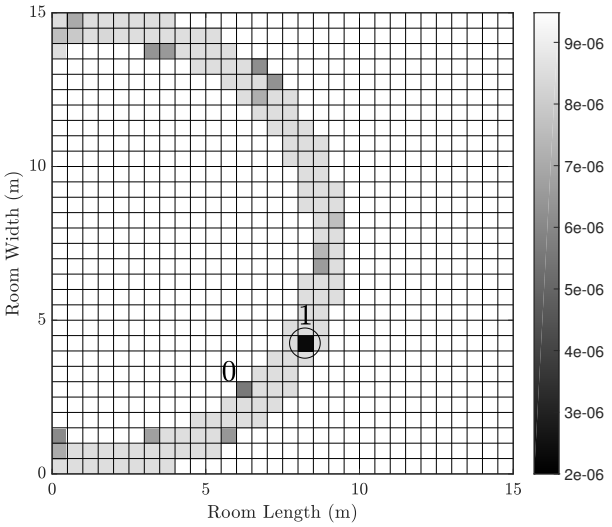

Fig. 16: The tiles that were obtained by the DHA, when used in the mm-Wave localization algorithm for $N_{DB} = 900$ tiles. The CF value of each evaluated tile is also plotted. The entries of the database that were not obtained during the DHA search have been fixed to a CF value of $9 \cdot 10^{-6}$, just for the sake of presentation, without meaning that their true CF value, presented in Fig. 12, has changed. The final output of each BBHT search during the DHA's process is numbered, in the sequence of the BBHT QSA occurrences. The circled tile is the closest to true position of the user. The last output of the last BBHT QSA's call, indicated by the number 1 is the output of the DHA and it is the correct tile. The unnumbered tiles denote the tiles that were measured by the BBHT QSAs but were not solutions, as expected by the trial-and-error procedure of the BBHT QSA.

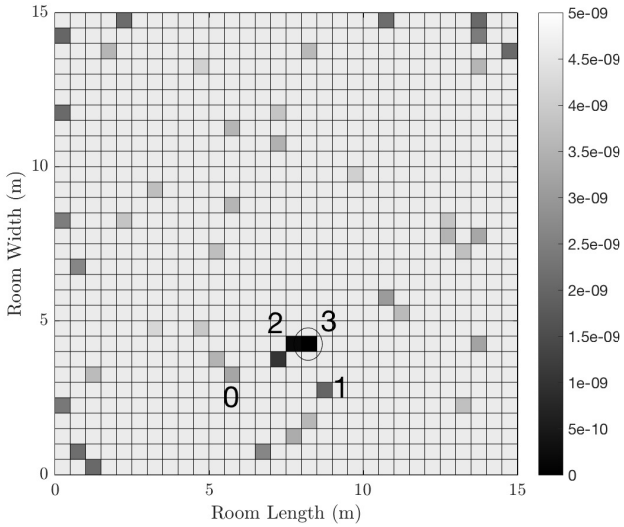

Fig. 17: The tiles that were obtained by the DHA, when used in the VLC fingerprinting localization algorithm for $N_{DB} = 900$ tiles. The CF value of each evaluated tile is also plotted. The entries of the database that were not obtained during the DHA search have been fixed to a CF value of $4.63 \cdot 10^{-9}$, just for the sake of presentation, without meaning that their true CF value, presented in Fig. 15, has changed. The final output of each BBHT search during the DHA's process is numbered, in the sequence of the BBHT QSA occurrences. The circled tile is the closest to true position of the user. The last output of the last BBHT QSA's call, indicated by the number 3 is the output of the DHA and it is the correct tile. The unnumbered tiles denote the tiles that were measured by the BBHT QSAs but were not solutions, as expected by the trial-and-error procedure of the BBHT QSA.

search, only the BBHT QSA can be used. However, when we measure the final quantum state at the end of the BBHT QSA, only one of the candidate quantum states will be obtained. By classically checking, whether the entry that corresponds to the index of the quantum state observed has a lower value than δ, we are able to determine whether there is an entry lower than δ or not. If there is, then that entry becomes the new δ and the same process is repeated, until the BBHT QSA is terminated without yielding an entry lower than δ. At that point we may conclude that the last δ we used is the minimum entry of the database and the DHA is concluded.

Since DHA employs the BBHT QSA, it also has a probabilistic complexity. The average complexity found for randomly constructed, unsorted databases was around $7\sqrt{N}$ database queries. The minimum complexity of $4.5\sqrt{N}$ is equal to the maximum complexity of the BBHT QSA and it corresponds to the particular scenario, where the minimum entry of the database was selected to be the initial input entry of the DHA. The maximum complexity of the database given by $22.5\sqrt{N}$ is rarely approached. In [28], we proposed an early termination criterion for the DHA. With the aid of this criterion we are able to tune its complexity, based on striking a trade-off between the affordable complexity budget and the success probability desired. Due to the methodology followed by the DHA, with the continuous updates of δ, even if the true minimum entry of the database is not found, an entry with a value close to that of the true minimum entry will have been obtained.

D. Localization Using Quantum Search Algorithms

In the localization problem, the search aims for finding the minimum entry in an unsorted database. Hence, the DHA may be employed for reducing the search complexity quantified in terms of the number of CFEs, while having a success probability of $\sim 100\%$. In both the mm-Wave and in the VLC localization algorithms, the average complexity of the DHA depends on the size of the database $N_{DB,\,mmW}$ and $N_{DB,\,VLC}$. For the same tile size, the database size in the mm-Wave localization algorithm is lower than that in the VLC localization algorithm $N_{DB,\,mmW} < N_{DB,\,VLC}$, due to the search space shrinking stage of Section II-E3. In the mm-Wave localization algorithm, the DHA performs a search for the minimum entry in the database consisting of $N_{DB,\,mmW}$ entries, which are constructed based on the CF

of (22). Similarly, in the VLC localization algorithm the DHA is employed for finding the minimum entry in a database of size $N_{DB,VLC} = N_T$, the entries of which are calculated based on (34).

When we employed the DHA in the scenario of Fig. 1 and the database of Fig. 12, where the database size is $N_{DB,mmW} = 126$, the resultant complexity was 52 CFEs. Only a certain fraction of the search space was retained after the measurements of the BBHT QSAs employed by the DHA, as illustrated in Fig. 16. For the same scenario, when using the VLC localization algorithm in the database of Fig. 15, 247 CFEs were required for identifying the specific tile that minimized the CF of (34). The tiles observed during the DHA search in the VLC localization algorithm are shown in Fig. 17. We may observe that in both localization algorithms, the required computational complexity is reduced, when the DHA is used instead of a full search. At the same time, the DHA succeeds in finding the correct tile in both the mm-Wave and the VLC localization algorithms.

When the DHA is used, the complexity reduction, quantified in terms of the percentage of the database size is improved when the database size is higher. This is the reason why in the mm-Wave localization algorithm the DHA requires 41.37% of the complexity needed by a full search in a database size of 126 entries, while it requires only 27.4% of the complexity imposed by the full search in a database size of 247 entries. Since the DHA's complexity is proportional to $\sqrt{N_{DB}}$, where N_{DF} is the size of the database, the higher the size of the database is, the higher the complexity reduction achieved by the DHA becomes.

Due to the nature of the mm-Wave-based localization algorithm, the database size differs, depending on the position of the user. At the same time, for the DHA to require a lower complexity than the full search, the database size should be higher than $2^6 = 64$ entries [28]. Therefore, in the mm-Wave localization methodology we will employ a hybrid quantum search for the "Exploring the Search Space" stage of Fig. 4, where a full search is performed if the size of the database is lower than 64 entries, while if the database size is higher than 64 entries, the DHA is used for finding the tile that corresponds to the minimum entry.

V. Simulation Results & Discussions

Let us now evaluate the localization methodologies and search algorithms investigated. Tables V and VI gather the values of all the parameters invoked by the mm-Wave-based and VLC-based localization algorithms, respectively. These remain unaltered in all the simulations. In all the simulations, we have moved a user to 90 000 different positions in the room, essentially moving a user on a grid with a step of 5 cm. We have employed a localization algorithm for each of these positions for 100 independent trials. We have also investigated the performance that different tile sizes offer, as well as different transmit power and antenna arrays. We have opted for using the maximum and average positioning error distance as our prime performance metric. For the mm-Wave-based localization algorithm, in contrast to the previous sections, an antenna array is installed on the ceiling in the center of the room, while for the VLC-based system, 64 APs are installed uniformly in the room. The reason we opted for a carrier frequency of $f_c = 28$ GHz with a bandwidth of 800 MHz, was both the availability of actual measurements of that system in [37], as well as the fact that in even higher frequencies, the associated high PLE for the NLOS paths increases the difficulty of detecting them. Nevertheless, the presented algorithm is applicable for a range of carrier frequencies.

TABLE V: mm-Wave Scenario Parameters

Number of anchors	$N_A = 1$
Anchor's position	$\mathbf{a}_0^{(1)} = [7.5,\ 7.5,\ 2.5]^T$
Height of Users	$0.85\ m$
Number of AEs	$M = 8$
Number of VAs	$L = 4$
Carrier frequency	$f_c = 28$ GHz
Bandwidth	$BW = 800\ MHz$
Sampling frequency	$f_s = 1600\ MHz$
Roll-off factor of RRC	$\beta = 0.5$
Path loss parameters	See Table IV
AE spacing in ULA	$d_{AE} = 5$ mm
Radius of the UCA	$r = 3.8\ mm$
AWGN power	$P_{w,dBm} = -174\ dBm/Hz$
SDNR	6 dB
Exponential decay constant	$\xi = 1.25\ ns$
Localization algorithm's	$N_p = 30$
design parameters	$N_{s,LOS} = 1$
	$N_{s,NLOS} = 5$

Figure 18 presents both the maximum and average positioning error for each of the 90 000 user positions, when the mm-Wave-based localization relied on the hybrid quantum search and a tile size of $(0.5\,m \times 0.5\,m)$, $EIRP = 25$ dBm. The resultant error pattern depends on the number of AEs installed on the UCA, as well as on the position of the UCA in the room. Based on the maximum positioning error recorded in Fig. 18a, the maximum error observed among all positions was 1.64 m, even though the relative frequency of observing such a high positioning error is very low, as it will be shown with the aid of probability density functions in our forthcoming analysis. A glimpse of this may be observed in Fig. 18b, which depicts the average positioning error for the same system, demonstrating that the average positioning error among all positions is 0.27 m. It should be noted that both Fig. 18a and Fig. 18b have been obtained using the same simulation instances and hence depend on the same random variable

This article has been accepted for publication in a future issue of this journal, but has not been fully edited. Content may change prior to final publication. Citation information: DOI 10.1109/ACCESS.2017.2733557, IEEE Access

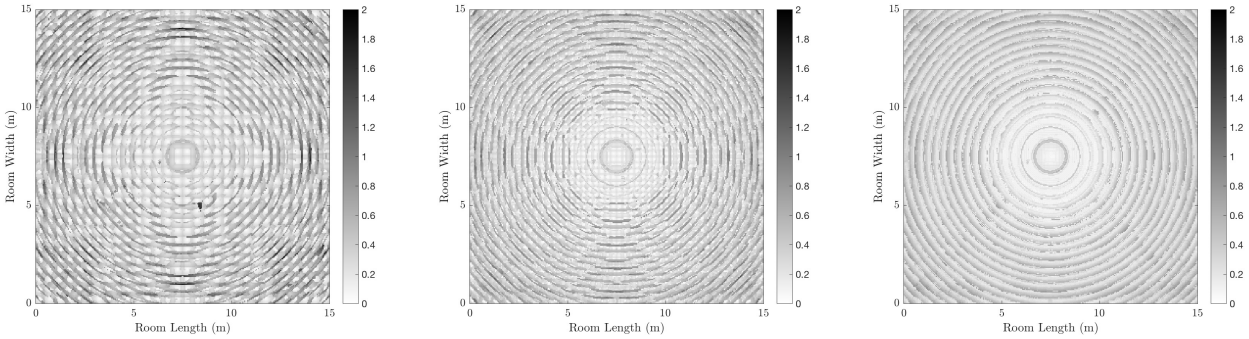

(a) Tile size: $(0.5\,m \times 0.5\,m)$.
Average error: 0.27 m.
Average complexity: 80 CFEs.

(b) Tile size: $(0.3\,m \times 0.3\,m)$.
Average error: 0.18 m.
Average complexity: 146 CFEs.

(c) Tile size: $(0.1\,m \times 0.1\,m)$.
Average error: 0.07 m.
Average complexity: 490 CFEs.

Fig. 20: Maximum positioning error, when using the mm-Wave localization methodology with hybrid quantum search for 90 000 user positions, three different tile sizes, $EIRP = 25$ dBm. The rest of the parameters are stated in Table V.

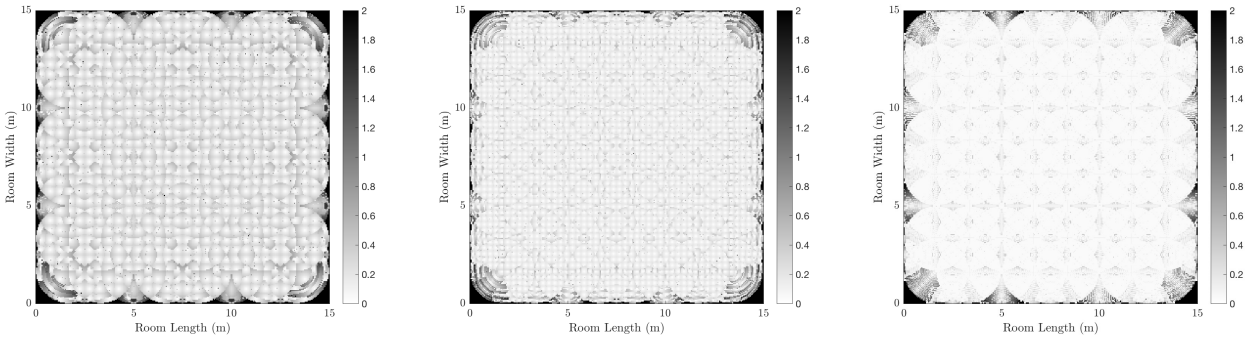

(a) Tile size: $(0.5\,m \times 0.5\,m)$.
Positions Lost: 1.12% (1010 positions).
Average error for found positions: 0.44 m.
Average complexity: 208 CFEs.
Average total error, assuming max error for lost positions: 0.67 m.

(b) Tile size: $(0.3\,m \times 0.3\,m)$.
Positions lost: 1.12% (1010 users).
Average error for found positions: 0.24 m.
Average complexity: 436 CFEs.
Average total error, assuming max error for lost positions: 0.46 m.

(c) Tile size: $(0.1\,m \times 0.1\,m)$.
Positions lost: 1.12% (1010 users).
Average error for found positions: 0.09 m.
Average complexity: 1293 CFEs.
Average total error, assuming max error for lost positions: 0.32 m.

Fig. 21: Maximum positioning error, when using the VLC localization methodology with DHA for 90 000 user positions and three different tile sizes. The rest of the parameters are stated in Table VI.

values. We may also conclude that the positioning error pattern is symmetric with respect to the center of the room, where the UCA is installed.

Still referring to Fig. 18, the average number of CFEs required for all tiles over all independent simulation instances by the hybrid quantum search was 80 CFEs. At the same time, if only a full search was performed for the databases, the average complexity would have been 139 CFEs, while the positioning error performance would be the same. In other words, the hybrid quantum search achieves the same performance as the full search, while requiring 57.5% of the CFEs. As we will show in a subsequent figure, this percentage will be even lower, when the tile size is reduced and hence the database size is increased.

Even though we used a ULA for our tutorial example, Fig. 19 suggests that a ULA should not be used in the mm-Wave-based localization algorithm, due to the inherent symmetry of the antenna array with respect to an axis. Hence, when a ULA is installed in the center of a symmetric room, the mm-Wave-based localization algorithm becomes unable to distinguish, whether the user is positioned on the left or on the right side of the ULA, since in both cases all AEs would have received exactly the same signals. All parameters' values in Fig. 19 are the same as those in Fig. 18. Therefore, in the following simulations we will employ a UCA for the mm-Wave-based localization.

When reducing the tile size, the positioning accuracy is expected to improve, since the grid's resolution is enhanced. This is evident in Fig. 20, where the maximum positioning error has been plotted for three different tile sizes, namely for $(0.5\,m \times 0.5\,m)$, $(0.3\,m \times 0.3\,m)$ and $(0.1\,m \times 0.1\,m)$, resulting in an average positioning error across all 90 000 user positions of 27 cm, 18 cm and 7 cm, respectively. When the "pencil-wide" beams of mm-Wave technology are used for communication, the more precise the localization, the less interference will be imposed on the adjacent users. Naturally, this comes at the price of an increased complexity, since by increasing the number of tiles, more CFEs are required by

This article has been accepted for publication in a future issue of this journal, but has not been fully edited. Content may change prior to final publication. Citation information: DOI 10.1109/ACCESS.2017.2733557, IEEE Access

TABLE VI: VLC Scenario Parameters

Number of APs	$N_{AP} = 64$
Height of APs	$2.5\ m$
Height of users	$0.85\ m$
Number of LEDs per AP	$60 \times 60 = 3600$
Center luminous intensity per LED	$I_0 = 350$ mcd
Transmitted optical power per LED	5.5 mW
Transmitted optical power per AP	$P_{T_x,opt} = 20$ W
Half of user's FOV	$\psi_c = 45^o$
Semi-angle at half power	$\phi_{1/2} = 60^o$
Physical area of photodetector	$A_r = 1\ cm^2$
Optical filter's gain	$T_s(\psi) = 1$
Refraction index	$n_{rfr} = 1.5$
Wall's reflection efficiency	$\rho = 0.75$
Wall's reflective area	$A_{wall} = 0.6875\ m^2$

both the full search and by the hybrid quantum search. More specifically, in order to achieve a 20 cm reduction in the average positioning error, from 27 cm to 7 cm, six times the number of CFEs is required on average.

When the 64 APs are employed for performing a VLC-based localization, the positioning accuracy also depends on the tile size and on the affordable complexity, as portrayed in Fig. 21, where the maximum recorded positioning error is illustrated for three different tile sizes. The main difference between the mm-Wave-based localization's performance of Fig. 20 and that of the VLC-based localization in Fig. 21, is that in the latter some user positions may never be found by the methodology, due to the visible light's limited coverage. As it may be seen close to the walls of the room, and especially at its four corners, there are 1010 positions, which are never found by the VLC-based localization. In other words, 1.12% of the 90 000 positions cannot be identified by the current system setup. By assigning the maximum possible positioning error of $15\sqrt{2} = 21.21$ m to them for our analysis, the average positioning error is 51 cm, 37 cm and 30 cm for the tile sizes of $(0.5\,m \times 0.5\,m)$, $(0.3\,m \times 0.3\,m)$ and $(0.1\,m \times 0.1\,m)$, respectively. If we only consider the specific positions that were in the coverage area, their average positioning error becomes 28 cm, 14 cm and 6 cm, respectively, for the three aforementioned tile sizes. Since in the VLC-based localization of Fig. 21 only the perturbations due to wall-reflections are assumed, if the user's position happens to be exactly at the center of a tile, its associated localization error may be equal to zero. None of the three tile sizes we used in Fig. 21 have a tile center exactly at a user's positions, in order to guarantee a fair comparison between the different tile sizes.

Still referring to Fig. 21, the average complexity required by the VLC-based localization using the DHA is 208 CFEs,

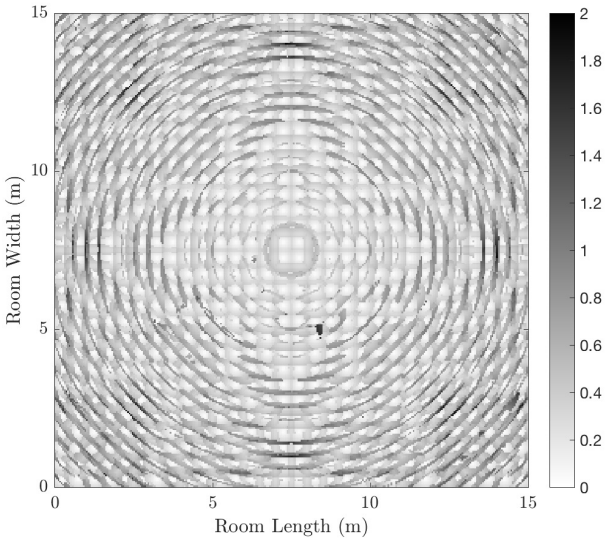

(a) Maximum Positioning Error

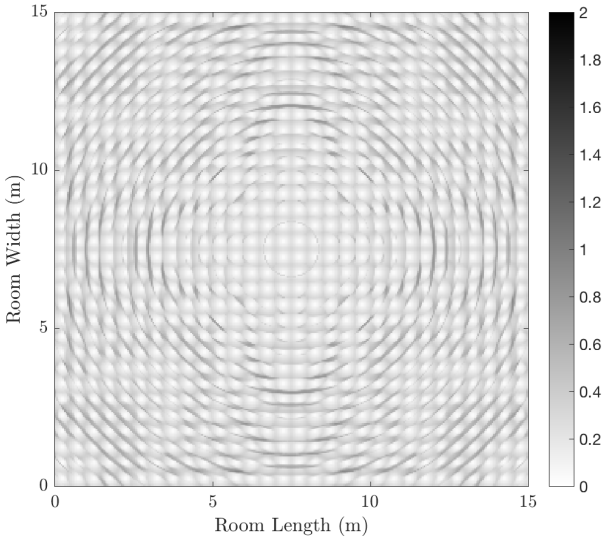

(b) Average Positioning Error

Fig. 18: Maximum and average positioning error of the mm-Wave-based localization, when a user is located in 90 000 different positions in the room and a UCA is installed at the center of the room, while the tile size is $(0.5\,m \times 0.5\,m)$. Furthermore, we have $EIRP = 25$ dBm. The rest of the parameters are gathered in Tables IV and V. The search complexity, averaged on all 90 000 positions, when the hybrid quantum search is employed is 80 CFEs, while that of the full search was 139 CFEs on average.

436 CFEs and 1293 CFEs, respectively, for the three tile sizes used. Comparing the complexities of the VLC-based localization for the three different tile sizes to the respective ones of the mm-Wave-based localization in Fig. 20, we may conclude that the mm-Wave-based localization achieves a similar performance in terms of the average positioning error over all the positions, while requiring fewer CFEs. Since the

This article has been accepted for publication in a future issue of this journal, but has not been fully edited. Content may change prior to final publication. Citation information: DOI 10.1109/ACCESS.2017.2733557, IEEE Access

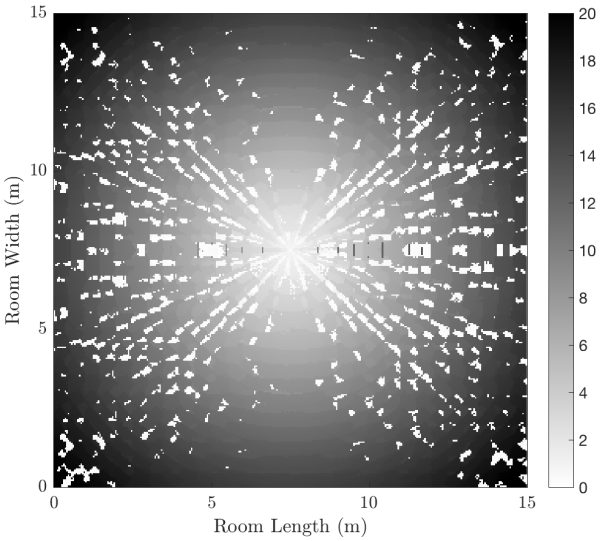

(a) Maximum Positioning Error

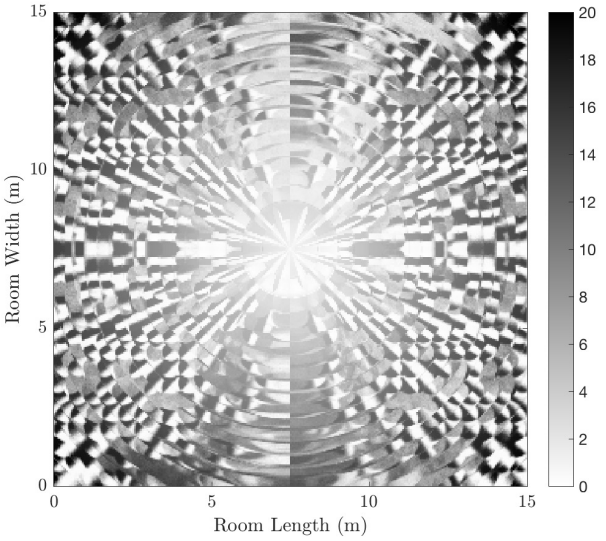

(b) Average Positioning Error

Fig. 19: Maximum and average error of the mm-Wave-based localization, when a user is located in 90 000 different positions in the room and a ULA is installed at the center of the room, while the tile size is $(0.5\,m \times 0.5\,m)$. Furthermore, we have $EIRP = 25$ dBm. The search complexity, averaged on all 90 000 positions, when the hybrid quantum search is employed is 80 CFEs, while that of the full search was 139 CFEs on average.

cost functions of the mm-Wave-based and the VLC-based localization methodologies are different, it may not be fair to compare them, but they both represent a single query of a database formed by the same tile arguments. Furthermore, in contrast to the VLC-based localization, the mm-Wave-based localization succeeds in localizing all user positions in the room.

The average positioning error's relation to the number

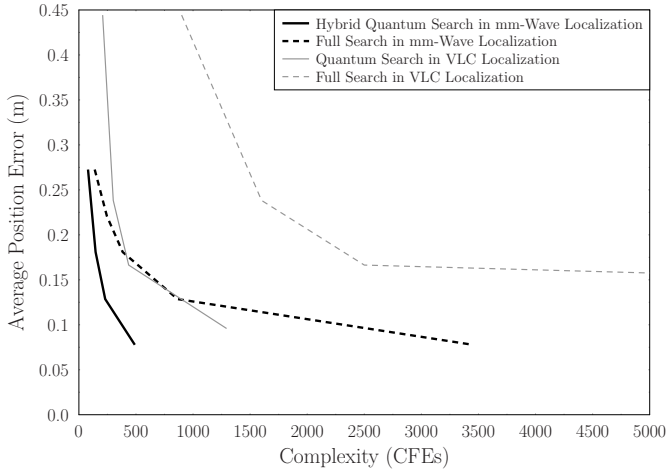

Fig. 22: Average positioning error among all user positions, with respect to the required computational complexity, in terms of the number of CFEs, for the mm-Wave-based and VLC-based localization methodologies, when a quantum search or a full search is performed. For the mm-Wave-based localization methodology, we have $EIRP = 25$ dBm. The rest of the parameters are gathered in Tables V and VI.

of CFEs required for both localization techniques may be better understood by observing Fig. 22. The complexity of both the mm-Wave-based and of the VLC-based localization methodologies was varied by only changing the tile size and the search algorithm. In both techniques, when a quantum search is used, we achieve a complexity reduction, which becomes even higher, when the complexity required by the full search is higher. In other words, the smaller the tile size of both localization methodologies, the higher the complexity reduction achieved by the quantum search becomes. For example, in order to achieve an average positioning error of 7 cm, the mm-Wave-based localization algorithm using the hybrid quantum search requires 14% of the number of CFEs required by a full search. Similarly, the VLC-based localization algorithm using the DHA requires 5.75% of the number of CFEs required by a full search for achieving an average positioning error of 9 cm. From another point of view, by investing the same complexity, a more precise localization can be achieved, when quantum search is used. For example, in the mm-Wave-based localization scenarios of Fig. 22, if the affordable complexity budget was 490 CFEs, by using a full search the average positioning error would be 16.9 cm, while the same error would be reduced to 7 cm, if the hybrid quantum search was used.

By comparing the quantum-search-aided mm-Wave-based and VLC-based localization methodologies in Fig. 22, assuming that their CFEs are equivalent in terms of power consumption, we may conclude that the mm-Wave based localization may achieve a similar average positioning error by requiring fewer CFEs than the VLC-based localization. This is due to the "Shrinking the Search Space" stage of the mm-Wave-based localization methodology of Section II-E3, which reduces the resultant search space. At the same time, the VLC-

This article has been accepted for publication in a future issue of this journal, but has not been fully edited. Content may change prior to final publication. Citation information: DOI 10.1109/ACCESS.2017.2733557, IEEE Access

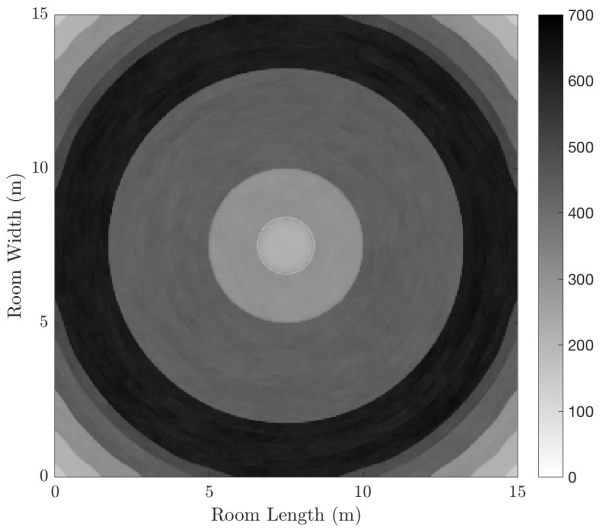

Fig. 23: Number of required CFEs among all user positions, when the mm-Wave-based localization is employed, with hybrid quantum search, $EIRP = 25$ dBm, and a tile size of $(0.1\,m \times 0.1\,m)$. The rest of the parameters are stated in Table V.

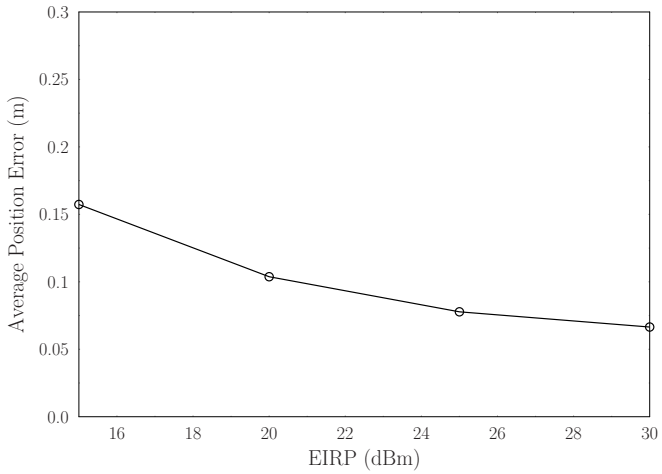

Fig. 24: Average positioning error among all user positions, with respect to the EIRP from the user, when the mm-Wave-based localization with hybrid quantum search, and a tile size of $(0.1\,m \times 0.1\,m)$ are employed. The rest of the parameters are stated in Table V.

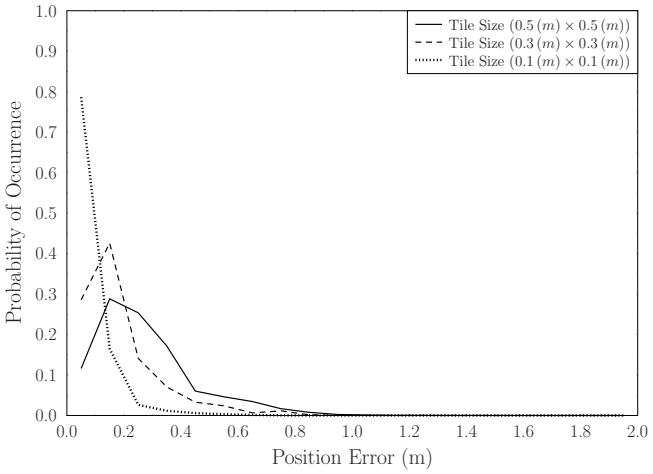

Fig. 25: Probability density function of the position error among all positions in the room for three different tile sizes in the mm-Wave based localization algorithm, where the hybrid quantum search was employed, $EIRP = 25$ dBm. The rest of the parameters are stated in Table V.

based localization methodology always performs a search right across the entire room. It should be noted that in Fig. 22, we have not taken into consideration during the calculation of the VLC-based localization's average positioning error, those specific user positions, which are out of coverage.

Recall that the "Shrinking the Search Space" stage of the mm-Wave-based localization methodology of Section II-E3 is based on the peaks estimated in the received power delay profile, as described in Section II-E2. In other words, it relies on the distance travelled by the received signals, without taking into consideration, which reflection caused which specular path. This is also illustrated in Fig. 23, which quantifies the computational complexity in terms of the number of CFEs, which is required at each user's position for the mm-Wave-based localization methodology, when the hybrid quantum search is used for a tile size of $(0.1\,m \times 0.1\,m)$. The complexity follows the trend of the number of tiles in the resultant database. If the shrinking stage was omitted, then the number of CFEs required would have been the same at all user positions.

Figure 24 depicts the effect of different EIRP levels on the average positioning error, when the mm-Wave-based localization relying on the hybrid quantum search is used and the tile size is $(0.1\,m \times 0.1\,m)$. As expected, by increasing the transmitted power, a lower average positioning error is achieved, which eventually reaches the minimum error floor, governed by the limited resolution of the room imposed by the selected tile size. Viewing Fig. 24 from another angle, by using a lower tile size and lower EIRP, we may achieve a similar performance to those scenarios, where a higher tile size combined with a higher EIRP was used. Therefore, depending on the localization precision required, on the power budgets of the users and on that of the physical anchor, a suitable allocation of transmission power and search complexity may be performed.

Figure 25 illustrates the probability density functions of the positioning error recorded for all positions in the room for three different tile sizes in the mm-Wave-based localization methodology using the hybrid quantum search. As expected, the probability of having a low position error is higher, when the tile size is small. The tails of the three probability distributions show that even though relatively high errors may be encountered, the probability of their occurrence is very low. For example, the probability of having an error close to 1.45 m is $3{\cdot}10^{-7}$, $3{\cdot}10^{-6}$ and $7.5{\cdot}10^{-5}$ for the tile size of $(0.1\,m{\cdot}0.1)$,

This article has been accepted for publication in a future issue of this journal, but has not been fully edited. Content may change prior to final publication. Citation information: DOI 10.1109/ACCESS.2017.2733557, IEEE Access

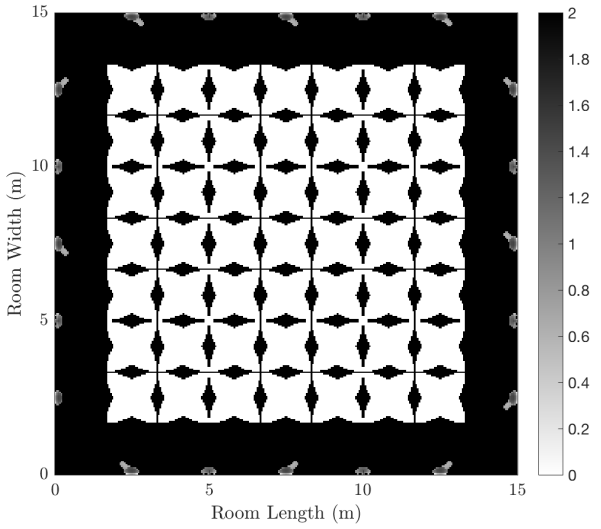

Fig. 26: Maximum positioning error of the VLC-based triangulation method, when a user is located in 90 000 different positions in the room, 64 APs for VLC are installed in the room. The system parameters are stated in Table VI.

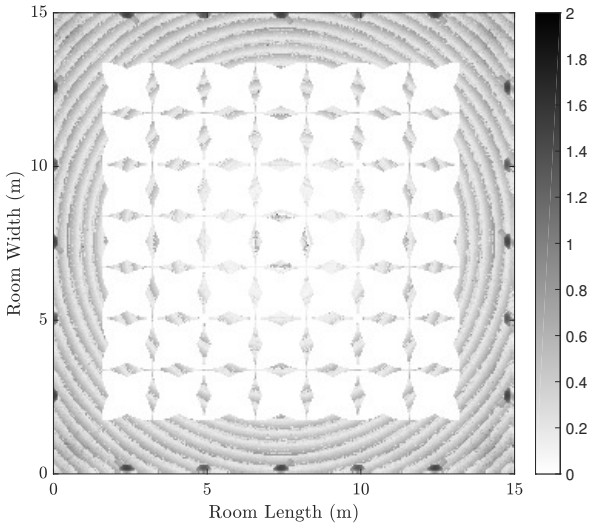

Fig. 27: Maximum positioning error of the joint VLC-based and mm-Wave-based localization, when a user is located in 90 000 different positions in the room, 64 APs for VLC are installed in the room and a UCA is installed at the center of the room. The VLC-based localization algorithm is employed first using the triangulation method. When a user is not found, the mm-Wave-based localization is used with hybrid quantum search, a tile size of $(0.1\,m \times 0.1\,m)$, $EIRP = 25$ dBm. The rest of the parameters are stated in Table V and Table VI. The average positioning error is 0.056 m and the average complexity is 261 CFEs.

$(0.3\,m \cdot 0.3)$ and $(0.5 \cdot 0.5)$, respectively. Therefore, even though Fig. 20 depicts the highest recorded positioning error for the three tile sizes, the probability distribution of the errors observed in Fig. 25 provides a more complete perspective on the mm-Wave-based localization's performance.

A. Joint VLC-based and mm-Wave-based Localization

Let us now join the forces between the downlink VLC-based and uplink mm-Wave-based localization, by employing the VLC-based localization using triangulation, as discussed in [5], and subsequently invoke mm-Wave-based localization, if the user happens to be out of the VLC coverage range. The presence of a user will be known due to its uplink transmissions. Hence, it is viable to assume that the system will know, when a user is present in the room, but he / she has not been localized by the VLC-based methodology. The triangulation method requires three APs in order to estimate the position of the user, similarly to the Global Positioning System (GPS). In our system, when the user receives signals from three APs, then VLC-based triangulation is performed, while in any other cases, the mm-Wave-based localization methodology using the hybrid quantum search and a tile size of $(0.1\,m \times 0.1\,m)$ is used.

The performance of the VLC-based triangulation alone is shown in Fig. 26. Naturally, since three APs are required for localizing the user, the number of positions, where the user is estimated by the VLC-based methodology is low. On the other hand, when triangulation is performed, the positioning error is close to zero, with the exception of the positions close to the four walls, where we have assumed in our simulations that the light is reflected, which allows triangulation to be used, albeit with a degraded result. Nevertheless, triangulation requires the overlap of coverage areas from different APs, therefore its success highly depends on the architecture of the room and on the density of the APs, as well as on the field of view.

When we allow the mm-Wave-based localization methodology to follow the VLC-based localization, by employing a UCA at the center of the room as in the previous scenarios, using hybrid quantum search and a tile size of $(0.1\,m \times 0.1\,m)$, the resultant performance is illustrated in Fig. 27. Since we employ both investigated systems sequentially, their maximum positioning error is related to the combination of Fig. 20c and Fig. 26. However, the average positioning error in the joint VLC-based and mm-Wave-based localization is 5.6 cm, which is lower than that of Fig. 20c, due to the improved localization precision offerred by the VLC-based triangulation in some parts of the room.

At the same time, assuming that the triangulation's complexity is much lower, than that of the fingerprinting method, we have assumed that no CFEs were required, when triangulation was employed. Therefore, the average number of CFEs required in Fig. 27 is 261 CFEs and all belong to the mm-Wave-based localization using the hybrid quantum search.

VI. Conclusions

In this contribution, we have proposed indoor localization algorithms for the uplink of mm-Wave communication systems, which rely on a single multi-antenna anchor and exploit the specular paths. In Section II we presented a tutorial on the

operation of this localization algorithm, while in Section IV we investigated the employment of quantum search algorithms for it, in order to reduce the number of CFEs required. Furthermore, we have used quantum search algorithms in the VLC-based localization methodology of Section III for achieving the same performance as the full search, while requiring lower complexity.

As illustrated in Fig. 18 and Fig. 19, we concluded that only the UCA, or two-dimensional antenna arrays, are suitable for the uplink mm-Wave localization methodology. In Fig. 20, we observed that by decreasing the size of the tiles in a fingerprinting method, the average positioning error diminishes, while the associated search complexity increases. The positioning error pattern in the room depends on a number of factors, such as the position of the anchor, the transmitted power and the number of AEs on the UCA. Similar conclusions were drawn for the VLC-based localization methodology in Fig. 21, which shows the positioning error for multiple tile sizes, when the DHA was used for conducting the search. The same figure shows that the VLC-based localization algorithm may be "blind" to specific user positions, due to its limited coverage. Therefore, the position of the APs is crucial for the performance of the VLC-based localization.

In Fig. 22 we compared the localization performance of both the uplink and downlink algorithms, when a quantum search algorithm is used and when only a classical full search is employed. We observed that when a quantum search algorithm is used for improving the localization, fewer CFEs are required for achieving the same performance as the full search. At the same time, assuming for the sake of comparison that the complexity of a single CFE in the mm-Wave-based localization methodology is equivalent to a single CFE in the VLC-based localization methodology, the uplink mm-Wave-based localization algorithm is able to offer a lower average positioning error across the room at a lower complexity, as observed in Fig. 22 for the two setups that we investigated. For example, if more APs were installed on the ceiling and especially close to the four walls, we expect the downlink VLC-based localization to outperform the uplink mm-Wave-based localization. Similarly, if more mm-Wave-enabled physical anchors are installed in the room, the localization estimation would improve.

As expected, based on Fig. 23, in the mm-Wave-based localization methodology, the required complexity depends on the user's position in the room due to the shrinking stage of the algorithm, as stated in Section II-E3. Furthermore, Fig. 24 illustrated the effect of different radiated powers on the average positioning error of the mm-Wave-based localization methodology. Since in Figs. 18, 19, 20 and 21 we referred to both the maximum observed and the average positioning error at each user's position, in Fig. 25, we plotted the probability distributions of the position error obtained by the mm-Wave-based localization methodology. More specifically, the maximum positioning error shown in Figs. 18, 19, 20 and 21 describes the worst-case scenario, but it has a very low probability of occurrence. At the same time, as expected, the position error probability distribution is shifted towards lower positioning errors, when the tile size is smaller. However, this comes with the cost of increased complexity.

Since the mm-Wave and VLC technologies are capable of operating at the same time in a given room the for uplink and downlink, respectively, we opted for joining their forces, instead of simply comparing their individual performances. Therefore, in Fig. 27 we presented the maximum positioning error observed, when the VLC-based triangulation of [5] is employed and if the user was not found, the mm-Wave-based localization methodology of Section II was activated. By employing this combined VLC and mm-Wave scheme, we were able to achieve a reduced average positioning error across all user positions in the room, while requiring fewer CFEs. The reason was that even though the downlink VLC-based triangulation achieves an infinitesimally low positioning error, it has a very limited coverage. This problem was eliminated, by using the uplink mm-Wave-based localization methodology.

Our future work includes the employment of multiple physical anchors in the mm-Wave-based localization methodology in order to further improve the localization accuracy. Moreover, we are aiming for exploiting the multiple AEs in the physical anchor of the mm-Wave-based localization methodology for further reducing the search space, before actually searching through it. This may allow us to achieve an even lower positioning error at the same complexity. Furthermore, in our treatise we only considered rooms, where there was no blockage. In reality, pillars and walls may block the LOS path, resulting in degraded localization accuracy. In our future work, we are planning to circumvent this problem by either employing multiple anchors, or exploiting the VAs in a different way. At the same time, we aim to use the estimated position as an initial step for a quantum-assisted tracking algorithm, which would follow the trajectory of each user. Finally, a joint VLC and mm-Wave localization algorithm, which would allow the exchange of information between the uplink and the downlink may prove beneficial.

REFERENCES

[1] S. Gezici, Z. Tian, G. B. Giannakis, H. Kobayashi, A. F. Molisch, H. V. Poor, and Z. Sahinoglu, "Localization Via Ultra-Wideband Radios: A Look at Positioning Aspects for Future Sensor Networks," *IEEE Signal Processing Magazine*, vol. 22, pp. 70–84, July 2005.

[2] A. Khalajmehrabadi, N. Gatsis, and D. Akopian, "Modern WLAN Fingerprinting Indoor Positioning Methods and Deployment Challenges," *IEEE Communications Surveys Tutorials*, vol. PP, no. 99, pp. 1–1, 2017.

[3] V. Degli-Esposti, F. Fuschini, E. M. Vitucci, M. Barbiroli, M. Zoli, L. Tian, X. Yin, D. A. Dupleich, R. Mller, C. Schneider, and R. S. Thom, "Ray-Tracing-Based mm-Wave Beamforming Assessment," *IEEE Access*, vol. 2, pp. 1314–1325, 2014.

[4] K. Witrisal, P. Meissner, E. Leitinger, Y. Shen, C. Gustafson, F. Tufvesson, K. Haneda, D. Dardari, A. F. Molisch, A. Conti, and M. Z. Win, "High-Accuracy Localization for Assisted Living: 5G systems will turn multipath channels from foe to friend," *IEEE Signal Processing Magazine*, vol. 33, pp. 59–70, March 2016.

[5] S. Feng, X. Li, R. Zhang, M. Jiang, and L. Hanzo, "Hybrid Positioning Aided Amorphous-Cell Assisted User-Centric Visible Light Downlink Techniques," *IEEE Access*, vol. 4, pp. 2705–2713, 2016.

[6] T. Lv, H. Gao, X. Li, S. Yang, and L. Hanzo, "Space-Time Hierarchical-Graph Based Cooperative Localization in Wireless Sensor Networks," *IEEE Transactions on Signal Processing*, vol. 64, pp. 322–334, Jan 2016.

[7] L. Hanzo, H. Haas, S. Imre, D. O'Brien, M. Rupp, and L. Gyongyosi, "Wireless Myths, Realities, and Futures: From 3G/4G to Optical and Quantum Wireless," *Proceedings of the IEEE*, vol. 100, no. Special Centennial Issue, pp. 1853–1888, 2012.

[8] F. Khan and Z. Pi, "mmWave Mobile Broadband (MMB): Unleashing the 3–300GHz Spectrum," in *IEEE Sarnoff Symposium*, pp. 1–6, May 2011.

[9] Z. Pi and F. Khan, "System Design and Network Architecture for a Millimeter-Wave Mobile Broadband (MMB) System," in *IEEE Sarnoff Symposium*, pp. 1–6, May 2011.

[10] T. Rappaport, S. Sun, R. Mayzus, H. Zhao, Y. Azar, K. Wang, G. Wong, J. Schulz, M. Samimi, and F. Gutierrez, "Millimeter Wave Mobile Communications for 5G Cellular: It Will Work!," *IEEE Access*, vol. 1, pp. 335–349, 2013.

[11] W. Roh, J. Y. Seol, J. Park, B. Lee, J. Lee, Y. Kim, J. Cho, K. Cheun, and F. Aryanfar, "Millimeter-Wave Beamforming as an Enabling Technology for 5G Cellular Communications: Theoretical Feasibility and Prototype Results," *IEEE Communications Magazine*, vol. 52, pp. 106–113, February 2014.

[12] I. A. Hemadeh, M. El-Hajjar, S. Won, and L. Hanzo, "Layered Multi-Group Steered Space-Time Shift-Keying for Millimeter-Wave Communications," *IEEE Access*, vol. 4, pp. 3708–3718, 2016.

[13] S. Rajagopal, R. D. Roberts, and S. K. Lim, "IEEE 802.15.7 Visible Light Communication: Modulation Schemes and Dimming Support," *IEEE Communications Magazine*, vol. 50, pp. 72–82, March 2012.

[14] C. X. Wang, F. Haider, X. Gao, X. H. You, Y. Yang, D. Yuan, H. M. Aggoune, H. Haas, S. Fletcher, and E. Hepsaydir, "Cellular Architecture and Key Technologies for 5G Wireless Communication Networks," *IEEE Communications Magazine*, vol. 52, pp. 122–130, February 2014.

[15] P. H. Pathak, X. Feng, P. Hu, and P. Mohapatra, "Visible Light Communication, Networking, and Sensing: A Survey, Potential and Challenges," *IEEE Communications Surveys Tutorials*, vol. 17, pp. 2047–2077, Fourthquarter 2015.

[16] A. ahin, Y. S. Erolu, . Gven, N. Pala, and M. Yksel, "Hybrid 3-D Localization for Visible Light Communication Systems," *Journal of Lightwave Technology*, vol. 33, pp. 4589–4599, Nov 2015.

[17] M. Biagi, S. Pergoloni, and A. M. Vegni, "LAST: A Framework to Localize, Access, Schedule, and Transmit in Indoor VLC Systems," *Journal of Lightwave Technology*, vol. 33, pp. 1872–1887, May 2015.

[18] K. Qiu, F. Zhang, and M. Liu, "Let the Light Guide Us: VLC-Based Localization," *IEEE Robotics Automation Magazine*, vol. 23, pp. 174–183, Dec 2016.

[19] A. Conti, M. Guerra, D. Dardari, N. Decarli, and M. Z. Win, "Network Experimentation for Cooperative Localization," *IEEE Journal on Selected Areas in Communications*, vol. 30, pp. 467–475, February 2012.

[20] H. Wymeersch, S. Marano, W. M. Gifford, and M. Z. Win, "A Machine Learning Approach to Ranging Error Mitigation for UWB Localization," *IEEE Transactions on Communications*, vol. 60, pp. 1719–1728, June 2012.

[21] P. Meissner and K. Witrisal, "Multipath-assisted single-anchor indoor localization in an office environment," in *International Conference on Systems, Signals and Image Processing (IWSSIP)*, pp. 22–25, April 2012.

[22] E. Leitinger, P. Meissner, C. Rdisser, G. Dumphart, and K. Witrisal, "Evaluation of Position-Related Information in Multipath Components for Indoor Positioning," *IEEE Journal on Selected Areas in Communications*, vol. 33, pp. 2313–2328, Nov 2015.

[23] C. Durr and P. Høyer, "A Quantum Algorithm for Finding the Minimum," *eprint arXiv:quant-ph/9607014*, July 1996.

[24] L. K. Grover, "A Fast Quantum Mechanical Algorithm for Database Search," *Proceedings, 28th Annual ACM Symposium on the Theory of Computing*, pp. 212–219, May 1996.

[25] L. K. Grover, "Quantum Mechanics Helps in Searching for a Needle in a Haystack," *Physical Review Letters*, vol. 79, pp. 325–328, July 1997.

[26] M. Boyer, G. Brassard, P. Høyer, and A. Tapp, "Tight Bounds on Quantum Searching," *Fortschritte der Physik*, vol. 46, pp. 493–506, 1998.

[27] P. Botsinis, S. X. Ng, and L. Hanzo, "Quantum Search Algorithms, Quantum Wireless, and a Low-Complexity Maximum Likelihood Iterative Quantum Multi-User Detector Design," *IEEE Access*, vol. 1, pp. 94–122, 2013.

[28] P. Botsinis, S. X. Ng, and L. Hanzo, "Fixed-Complexity Quantum-Assisted Multi-User Detection for CDMA and SDMA," *IEEE Transactions on Communications*, vol. 62, pp. 990–1000, March 2014.

[29] P. Botsinis, D. Alanis, S. X. Ng, and L. Hanzo, "Low-Complexity Soft-Output Quantum-Assisted Multiuser Detection for Direct-Sequence Spreading and Slow Subcarrier-Hopping Aided SDMA-OFDM Systems," *IEEE Access*, vol. 2, pp. 451–472, May 2014.

[30] P. Botsinis, D. Alanis, Z. Babar, S. X. Ng, and L. Hanzo, "Noncoherent Quantum Multiple Symbol Differential Detection for Wireless Systems," *IEEE Access*, vol. 3, pp. 569–598, May 2015.

[31] P. Botsinis, D. Alanis, Z. Babar, S. Ng, and L. Hanzo, "Iterative Quantum-Assisted Multi-User Detection for Multi-Carrier Interleave Division Multiple Access Systems," *IEEE Transactions on Communications*, vol. 63, pp. 3713–3727, July 2015.

[32] P. Botsinis, D. Alanis, Z. Babar, H. V. Nguyen, D. Chandra, S. X. Ng, and L. Hanzo, "Quantum-Aided Multi-User Transmission in Non-Orthogonal Multiple Access Systems," *IEEE Access*, vol. 4, pp. 7402–7424, 2016.

[33] P. Botsinis, D. Alanis, Z. Babar, S. X. Ng, and L. Hanzo, "Joint Quantum-Assisted Channel Estimation and Data Detection," *IEEE Access*, vol. 4, pp. 7658–7681, 2016.

[34] D. Alanis, P. Botsinis, Z. Babar, S. X. Ng, and L. Hanzo, "Non-Dominated Quantum Iterative Routing Optimization for Wireless Multihop Networks," *IEEE Access*, vol. 3, pp. 1704–1728, 2015.

[35] D. Alanis, J. Hu, P. Botsinis, Z. Babar, S. X. Ng, and L. Hanzo, "Quantum-Assisted Joint Multi-Objective Routing and Load Balancing for Socially-Aware Networks," *IEEE Access*, vol. 4, pp. 9993–10028, 2016.

[36] P. Botsinis, Z. Babar, D. Alanis, D. Chandra, H. Nguyen, S. X. Ng, and L. Hanzo, "Quantum error correction protects quantum search algorithms against decoherence," *Scientific Reports*, vol. 6, no. 38095, 2016.

[37] G. R. Maccartney, T. S. Rappaport, S. Sun, and S. Deng, "Indoor Office Wideband Millimeter-Wave Propagation Measurements and Channel Models at 28 and 73 GHz for Ultra-Dense 5G Wireless Networks," *IEEE Access*, vol. 3, pp. 2388–2424, 2015.

[38] P. Ioannides and C. A. Balanis, "Uniform Circular Arrays for Smart Antennas," *IEEE Antennas and Propagation Magazine*, vol. 47, pp. 192–206, Aug 2005.

[39] J. G. Proakis, *Digital Communications*. McGraw-Hill, 1995.

[40] J. Pascual-Garca, J. M. Molina-Garca-Pardo, M. T. Martnez-Ingls, J. V. Rodrguez, and N. Saurn-Serrano, "On the Importance of Diffuse Scattering Model Parameterization in Indoor Wireless Channels at mm-Wave Frequencies," *IEEE Access*, vol. 4, pp. 688–701, 2016.

[41] K. Haneda, J. Jrvelinen, A. Karttunen, M. Kyr, and J. Putkonen, "A Statistical Spatio-Temporal Radio Channel Model for Large Indoor Environments at 60 and 70 GHz," *IEEE Transactions on Antennas and Propagation*, vol. 63, pp. 2694–2704, June 2015.

[42] N. Michelusi, U. Mitra, A. F. Molisch, and M. Zorzi, "UWB Sparse/Diffuse Channels, Part I: Channel Models and Bayesian Estimators," *IEEE Transactions on Signal Processing*, vol. 60, pp. 5307–5319, Oct 2012.

[43] N. Czink, A. Richter, E. Bonek, J. P. Nuutinen, and J. Ylitalo, "Including Diffuse Multipath Parameters in MIMO Channel Models," in *IEEE Vehicular Technology Conference*, pp. 874–878, Sept 2007.

[44] T. Komine and M. Nakagawa, "Fundamental Analysis for Visible-Light Communication System Using LED Lights," *IEEE Transactions on Consumer Electronics*, vol. 50, pp. 100–107, Feb 2004.

[45] M. A. Nielsen and I. L. Chuang, *Quantum Computation and Quantum Information*. Cambridge University Press, 2000.

[46] S. Imre and F. Balázs, *Quantum Computing and Communications: An Engineering Approach*. John Wiley & Sons, 2005.

[47] S. Imre and L. Gyongyosi, *Advanced Quantum Communications: An Engineering Approach*. John Wiley & Sons, 2013.

Panagiotis Botsinis (S'12-M'15) received the M.Eng. degree from the School of Electrical and Computer Engineering of the National Technical University of Athens (NTUA), Greece, in 2010, as well as the M.Sc. degree with distinction and the Ph.D. degree in Wireless Communications from the University of Southampton, UK, in 2011 and 2015, respectively. He is currently working as a Research Fellow in the Southampton Wireless group at the School of Electronics and Computer Science of the University of Southampton, UK. Since October 2010, he has been a member of the Technical Chamber of Greece.

His research interests include quantum-assisted communications, quantum computation, iterative detection, OFDM, MIMO, multiple access systems, coded modulation, channel coding, cooperative communications, as well as combinatorial optimization.

This article has been accepted for publication in a future issue of this journal, but has not been fully edited. Content may change prior to final publication. Citation information: DOI 10.1109/ACCESS.2017.2733557, IEEE Access

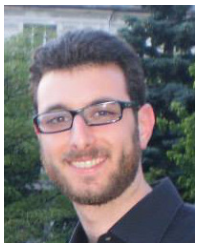

Dimitrios Alanis (S'13) received the M.Eng. degree in Electrical and Computer Engineering from the Aristotle University of Thessaloniki in 2011 and the M.Sc. degree in Wireless Communications from the University of Southampton in 2012. He is currently working towards the PhD degree with the Southampton Wireless (SW) Group, School of Electronics and Computer Science of the University of Southampton.

His research interests include quantum computation and quantum information theory, quantum search algorithms, cooperative communications, resource allocation for self-organizing networks, bio-inspired optimization algorithms and classical and quantum game theory.

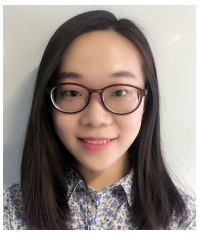

Simeng Feng received her B.Eng degree in Electronic Information Science and Technology from Ocean University of China and received her Master degree in Wireless Communications from University of Southampton, UK. Now, she is working towards her Ph.D. degree with Southampton Wireless, University of Southampton, UK.

Her research interests include visible light communications, optical modulations, indoor positioning, amorphous cells, heterogeneous networks and energy efficiency.

Zunaira Babar received her B.Eng. degree in electrical engineering from the National University of Science & Technology (NUST), Islamabad, Pakistan, in 2008, and the M.Sc. degree (Distinction) and the Ph.D degree in wireless communications from the University of Southampton, UK, in 2011 and 2015, respectively. She is currently working as a Research Fellow in the Southampton Wireless group at the University of Southampton.

Her research interests include quantum error correction codes, channel coding, coded modulation, iterative detection and cooperative communications.

Hung Viet Nguyen received the B.Eng. degree in Electronics & Telecommunications from Hanoi University of Science and Technology (HUST), Hanoi, Vietnam, in 1999, the M.Eng. in Telecommunications from Asian Institute of Technology (AIT), Bangkok, Thailand, in 2002 and the Ph.D. degree in wireless communications from the University of Southampton, Southampton, U.K., in 2013. Since 1999 he has been a lecturer at the Post & Telecommunications Institute of Technology (PTIT), Vietnam. He is involved in the OPTIMIX and CONCERTO European projects. He is currently a postdoctoral researcher at Southampton Wireless (SW) group, University of Southampton, UK.

His research interests include cooperative communications, channel coding, network coding and quantum communications.

Daryus Chandra (S'13) received the M.Eng. degree in electrical engineering from Universitas Gadjah Mada (UGM), Indonesia, in 2014. He is currently pursuing the Ph.D degree with the Southampton Wireless group, School of Electronics and Computer Science, University of Southampton. He is a recipient of scholarship award from Indonesia Endowment Fund for Education (LPDP).

His research interests includes channel codes, quantum error correction codes, and quantum communications.

Soon Xin Ng (S'99-M'03-SM'08) received the B.Eng. degree (First class) in electronics engineering and the Ph.D. degree in wireless communications from the University of Southampton, Southampton, U.K., in 1999 and 2002, respectively. From 2003 to 2006, he was a postdoctoral research fellow working on collaborative European research projects known as SCOUT, NEWCOM and PHOENIX. Since August 2006, he has been a member of academic staff in the School of Electronics and Computer Science, University of Southampton. He is involved in the OPTIMIX and CONCERTO European projects as well as the IUATC and UC4G projects. He is currently an Associate Professor of Telecommunications with the University of Southampton. He has authored over 180 papers and co-authored two John Wiley/IEEE Press books in his research field.

His research interests include adaptive coded modulation, coded modulation, channel coding, space-time coding, joint source and channel coding, iterative detection, OFDM, MIMO, cooperative communications, distributed coding, quantum error correction codes and joint wireless-and-optical-fiber communications. He is a a Chartered Engineer and a Fellow of the Higher Education Academy in the UK.

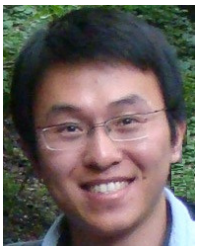

Rong Zhang (M'09-SM'16) is an assistant professor in Southampton Wireless group within the school of ECS at University of Southampton (UoS). He received his PhD in wireless communications from UoS in 2009, where he was a research assistant during that period with Mobile Virtual Centre of Excellence, one of UK's largest industrial-academic partnership in ICT. During his post-doctoral period in ECS, he contributed as the UoS lead researcher on a number of international projects. After that, he took his industrial consulting leave for Huawei EU R& D as a System Algorithms Expert. He has a total of 80+ IEEE/OSA publications, including 55+ journals (20+ of which as first author). Owing to his outstanding academic achievements, he is the recipient of the prestigious Dean's Publication Award. He is also the recipient of the prestigious RAEng industrial fellowship. He regularly serves as reviewer for IEEE/OSA journals and funding bodies and has been several times as TPC member/invited session chair of major conferences. He is a RAEng industrial fellow, a senior member of the IEEE, a member of the OSA.

Lajos Hanzo (M'91-SM'92-F'04) received his degree in electronics in 1976 and his doctorate in 1983. In 2009 he was awarded the honorary doctorate "Doctor Honoris Causa" by the Technical University of Budapest. During his 38-year career in telecommunications he has held various research and academic posts in Hungary, Germany and the UK. Since 1986 he has been with the School of Electronics and Computer Science, University of Southampton, UK, where he holds the chair in telecommunications. He has successfully supervised about 100 PhD students, co-authored 20 John Wiley/IEEE Press books on mobile radio communications totalling in excess of 10,000 pages, published 1,500+ research entries at IEEE Xplore, acted both as TPC and General Chair of IEEE conferences, presented keynote lectures and has been awarded a number of distinctions. Currently he is directing a 100-strong academic research team, working on a range of research projects in the field of wireless multimedia communications sponsored by industry, the Engineering and Physical Sciences Research Council (EPSRC) UK, the European Research Council's Advanced Fellow Grant and the Royal Society's Wolfson Research Merit Award. He is an enthusiastic supporter of industrial and academic liaison and he offers a range of industrial courses.

Lajos is a Fellow of the Royal Academy of Engineering, of the Institution of Engineering and Technology, and of the European Association for Signal Processing. He is also a Governor of the IEEE VTS. During 2008-2012 he was the Editor-in-Chief of the IEEE Press and a Chaired Professor also at Tsinghua University, Beijing. He has 22,000+ citations. For further information on research in progress and associated publications please refer to http://www-mobile.ecs.soton.ac.uk.